Limestone Coast Airborne Electromagnetic Survey:
Acquisition, Processing and Modelling

Aaron Davis, Tim Munday, and Tania Ibrahimi

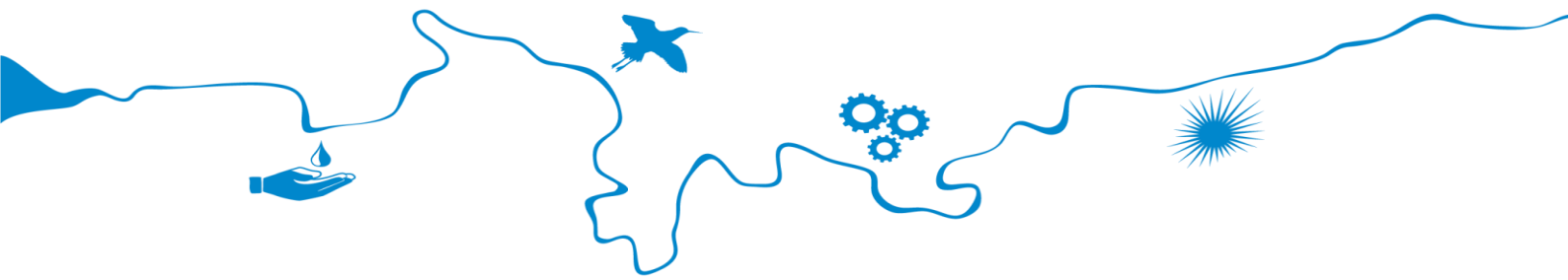

Goyder Institute for Water Research
Technical Report Series No. 25/5.1

www.goyderinstitute.org

Goyder Institute for Water Research Technical Report Series ISSN: 1839-2725

The Goyder Institute for Water Research is a research alliance between the South Australian Government through the Department for Environment and Water, CSIRO, Flinders University, the University of Adelaide and the University of South Australia. The Institute facilitates governments, industries, and leading researchers to collaboratively identify, develop and adopt innovative solutions for complex water management challenges to ensure a sustainable future.

Enquires should be addressed to: Goyder Institute for Water Research
The University of Adelaide (Manager)
209A, Level 2 Darling Building, North Terrace,
Adelaide, SA 5000
tel: (08) 8313 5020
e-mail: enquiries@goyderinstitute.org

Citation

Davis A, Munday TJ, and Ibrahimi T (2025) Limestone Coast Airborne Electromagnetic Survey: Acquisition, Processing and Modelling. Goyder Institute for Water Research Technical Report Series No. 25/5.1

Disclaimer

This report has been prepared by the CSIRO, Flinders University and the Lower Limestone Coast Landscape Board and reviewed in accordance with the publication protocols of the Goyder Institute for Water Research. The report contains independent scientific/technical advice to inform government decision-making. The independent findings and recommendations of this report are subject to separate and further consideration and decision-making processes and do not necessarily represent the views of the Australian Government, South Australian Department for Environment and Water or the Limestone Coast Landscape Board. The Goyder Institute and its partner organisations do not warrant or make any representation regarding the use, or results of the use, of the information contained herein about its correctness, accuracy, reliability, currency or otherwise and expressly disclaim all liability or responsibility to any person using the information or advice. Information contained in this document is, to the knowledge of the project partners, correct at the time of writing.

Contents

Figures

Tables

First Nations Respect and Reconciliation

The Goyder Institute for Water Research and Limestone Coast Landscape Board, acknowledges the Traditional Custodians of the lands and waters of the Limestone Coast and South East region, where this project took place. Together we pay our respects to their Elders—past, present, and emerging—and recognise Aboriginal people as the First Peoples and Nations of South Australia, possessing and caring for these lands under their own laws and customs.

We respect the enduring cultural, spiritual, physical, and emotional connections that Aboriginal peoples maintain with their lands and waters. We recognise the diverse rights, interests, and obligations of First Nations and the deep cultural connections that exist between different First Nations communities. We seek to support their meaningful engagement and honour the continuation of their cultural heritage, economies, languages, and laws, which remain of ongoing importance.

We walk together with the First Nations of the South East and the Ngarrindjeri peoples through organisations such as Burrandies Aboriginal Corporation, Ngarrindjeri Aboriginal Corporation, the Ngarrindjeri Lands & Progress Aboriginal Corporation and South East Aboriginal Focus Group. For the work of generations past, and the benefit of generations future, we seek to be a voice for reconciliation in all that we do.

Project Summary

The Limestone Coast of South Australia is a highly modified landscape with an extensive cross-catchment drainage system converting what was once a wetland dominated landscape into one dominated by agricultural production. The region now has a diverse agricultural sector and extensive forestry plantations which are highly dependent on reliable rainfall and easy access to the region's substantial groundwater resources. However, as climatic conditions become hotter and drier it's important to understand impacts on ground and surface water resources and consequent risks to primary production and the environment to build a water secure future.

Achieving water security in the Limestone Coast region under a changing climate requires a more integrated and holistic approach to water resource management. In particular, the interactions between surface water and groundwater must be better understood, quantified, and managed to balance the seasonal demands—removing excess water from productive lands during winter while safeguarding groundwater-dependent agriculture and ecosystems during summer.

The "Adaptation of the South Eastern Drainage Network under a changing climate" project aims to inform opportunities to improve water management in the region - including potential use of water in the drainage network - to address risks to primary industries and groundwater dependent ecosystems. Delivered through the Goyder Institute for Water Research, research teams from the CSIRO, Flinders University and the University of South Australia have completed five separate but inter-connected tasks:

1. Quantifying the value of consumptive and non-consumptive uses of water.

This task assessed the value of additional water for key primary industries in the region, while also estimating the value of water for non-consumptive uses aimed at achieving ecological outcomes. Together, these valuations provide important context to the project's hydrological tasks, informing options to manage additional available water in the region.

2. Current and future water availability.

A water balance model for the region has been developed using the Bureau of Meteorology's Australian Water Resources Assessment – Landscape (AWRA-L) model. It integrates national and regional datasets to capture surface runoff, recharge, and soil moisture, while accounting for seasonal dynamics and regional variability. The model enables analysis of climate change impacts on the full water balance, providing insight into future water availability, supporting both short- and long-term water management decisions.

3. Modelling groundwater and wetland interaction.

Site-specific models representing three-dimensional aquifer-wetland interactions have been developed for two key groundwater dependent sites. The models test the feasibility of changing the water distribution in the local landscape to improve ecosystem health and mitigate impacts of groundwater extraction. Options included redirecting / holding water back in drains, altering surface water inflows and reducing the extent of the wetland basin with levees. The learnings from modelling these two disparate sites will assist decisions to manage additional available water in the region.

4. Sea water intrusion risk.

The coastal area south of Mount Gambier is an area of high value irrigated agriculture and significant karst springs where the risk of seawater intrusion is of concern for both irrigators and environmental assets. This task set out to understand the extent and hydrodynamics of seawater intrusion in the region with an airborne electromagnetic survey of the south coast area, undertaken in October 2022, and construction of cross-sectional models to simulate seawater intrusion under different scenarios at different regional locations. This work provides the evidential basis to build on previous projects where reinstating wetlands by retaining water in drains appeared to effect some control over the seawater interface.

5. Groundwater, Ecology, Surface water and Wetland Assessment Tool (GESWAT)

To enable opportunities to improve water management to be easily identified and investigated - including the potential use of water in the drainage network –a dynamic GIS tool (GESWAT) was built. GESWAT brings

together outputs from the other project tasks integrating them in a tool with a range of other critical data (e.g. surface water flows, groundwater levels, and rainfall data, annual water use and allocation data, ecological information and other standard datasets). GESWAT provides the LC Landscape Board and its partner agencies a single platform with which to view, compare and interrogate the diversity of hydrological and ecological information available to inform policy and management decisions.

This report details results from Task 1 of the project.

Further results from this project are presented in the following reports:

Task 1

Cooper, C., Crase, L., Kandulu, J., and Subroy, V. (2025) Adaptation of the South-Eastern drainage system under a changing climate - Quantifying the value of different water uses and future demands. Goyder Institute for Water Research Technical Report Series No. 25/2

Task 2

Gibbs, M.S., Montazeri, M., Wang, B., Crosbie, R., Yang, A. (2025) Adaptation of the South-Eastern drainage system under a changing climate - Water Availability for South East Drainage Adaptation. Goyder Institute for Water Research Technical Report Series No. 25/3

Task 3

Gholami, A., Werner, A.D., Maskooni, E.K., Fan, H., Jazayeri, A., and Solórzano-Rivas, C. (2025) Adaptation of the South-Eastern drainage system under a changing climate - Groundwater and wetland modelling. Goyder Institute for Water Research Technical Report Series No. 25/4

Task 4

Davis A, Munday TJ, and Ibrahimi T (2025) Adaptation of the South-Eastern drainage system under a changing climate - Limestone Coast Airborne Electromagnetic Survey: Acquisition, Processing and Modelling. Goyder Institute for Water Research Technical Report Series No. 25/5.1

Davis A, Munday TJ, and Ibrahimi T (2025) Adaptation of the South-Eastern drainage system under a changing climate - Limestone Coast Airborne Electromagnetic Survey: Modelling Results. Goyder Institute for Water Research Technical Report Series No. 25/5.2

Gholami, A., Werner, A.D., Solórzano-Rivas, C., Jazayeri, A., Maskooni, E.K., and Hongxiang, F. (2025) Adaptation of the South-Eastern drainage system under a changing climate - Seawater intrusion risk. Goyder Institute for Water Research Technical Report Series No. 25/5.3

Task 5

Gonzalez, D., Werner, A., Jazayeri, A., Pritchard, J., Hongxiang, F., Botting, S., Judd, R. (2025) Adaptation of the South-Eastern drainage system under a changing climate - Groundwater, Ecology, Surface water and Wetland Assessment Tool (GESWAT) Spatial Data Dictionary. Goyder Institute for Water Research Technical Report Series No. 25/6

Executive Summary

Water planning and adaption actions linked to irrigated agriculture along the South Coast of South Australia are hindered by a limited understanding of the spatial extent and variability of the saltwater interface (SWI) along its extent. This report represents a contribution to our understanding of the risk posed to irrigated agriculture by saltwater intrusion along the coast. Specifically, it details the acquisition of airborne electromagnetic data, a geophysical technology, that can remotely define the subsurface electrical conductivity structure of the area flown. Data from these systems can then be used to map the three-dimensional extent and geometry of salt water as it interacts with groundwater in coastal aquifers.

In mid-2022, just over 1200-line kilometers of AEM data were in a series of flight lines which crossed the coast from Lake Bonney to the South Australian- Victorian Border, including the Piccaninnie Ponds Conservation Park.

This report describes the principles involved in the acquisition of these airborne electromagnetic data and the procedures required to generate an accurate three-dimensional conductivity model of the subsurface electrical structure. The AEM survey and the resulting modelled conductivity structure suggests a complex interaction between the regional groundwater system, lithology and the ocean. This is illustrated by the irregularity of the saltwater interface along this stretch of the coast, and particularly the unevenness of its ingress inland.

This study was undertaken between October 2022 to June 2025.

Funding and Delivery Statement

This *Adaptation of the SE drainage system to a changing climate* project has been jointly funded by the Australian Government through the National Water Grid Authority, the Limestone Coast Landscape Board, and the South Australian Government. The project was delivered by the Goyder Institute for Water Research partners: CSIRO, the University of South Australia, Flinders University and the University of Adelaide in collaboration with the Limestone Coast Landscape Board, South Eastern Water Conservation and Drainage Board (SEWCD Board) and the Department for Environment and Water. This report was prepared by Aaron Davis, Tim Munday and Tania Ibrahimi.

1 Introduction

Water planning and adaption actions linked to irrigated agriculture along the South Coast of South Australia are hindered by a limited understanding of the spatial extent and variability of the saltwater interface (SWI) along its extent. This report represents a contribution to an understanding of the risk posed to irrigated agriculture by saltwater intrusion along the coast. Specifically, it covers the acquisition, processing and modelling of airborne electromagnetic (AEM) data to determine the spatial extent, geometry and continuity of the saltwater interface in the region covered. A description of the technology used, and the methods employed provide context for the results presented.

1.1 Problem definition

Key management questions that will be addressed using the information generated from the AEM survey include:

- What is the landward extent and geometry of the saltwater interface (SWI) across the region?
- What is the relationship between the coastal aquifers, their properties and the saltwater interface?

1.2 Summary of previous investigations and knowledge gaps limiting management

Previous work in the region (e.g. Mustafa et al., 2012) noted that the risk of seawater intrusion into the coastal aquifer in the region had not been studied in detail and there was insufficient monitoring infrastructure available to adequately determine the risk posed to GDEs and agriculture in the coastal zone of the Lower Southeast. They also noted that the advent of large-scale irrigation using centre pivots in the 1990s, resulted in increasing extractions in near coastal areas, meaning that the risk of seawater intrusion into the regional unconfined aquifer became greater. Investigation into this possibility was listed as a high priority by the Southeast Natural Resources Management (NRM) Board.

Airborne geophysical data, specifically airborne electromagnetic (AEM) data provide an effective, non-intrusive means, for assessing the SWI in coastal settings and its potential to be a threat to current land use. Airborne electromagnetics has been used in numerous studies of coastal areas to image the interaction between fresh aquifer systems that are affected by seawater intrusion. The strong conductivity contrast between fresh and saline water makes it a relatively easy target to define using electromagnetic methods. Examples of the applicability of the technology for defining the SWI includes the work of Kirkegaard et al. (2011), Jørgensen et al. (2012), Annetts et al. (2015) and Pedersen et al. (2017). More recently, Goebel et al. (2019) used the SkyTEM AEM system, similar to that used for this study, to define the geometry of the saltwater interface data in northern part of Monterey Bay, in California, USA.

1.3 Approach to addressing key knowledge gaps and management questions

Through the acquisition and inversion of airborne electromagnetic data, this study aimed to generate a new model of the spatial extent, geometry and continuity of the saltwater interface along the South coast. In turn, this will provide baseline information on the current extent of saltwater intrusion into the coast, thereby assisting models to manage the risk.

The approach involved the acquisition of heli-borne airborne electromagnetic data along short survey lines orientated perpendicular to the coast (see section 2.2). A helicopter survey was also preferred to address the need for relatively high resolution near surface and deep information on the subsurface conductivity structure.

2 Airborne electromagnetic survey

2.1 Principles of AEM data acquisition

EM surveying techniques involve the measurement of the varying response of the ground due to the propagation of electromagnetic fields. Primary fields are generated by passing a current through a loop or coil positioned in the air, referred to as the transmitter loop (see Figure 2-1). A secondary field is induced in the ground and these fields are detected by the alternating currents that are induced to flow in a receiver coil by a process known as electromagnetic induction.

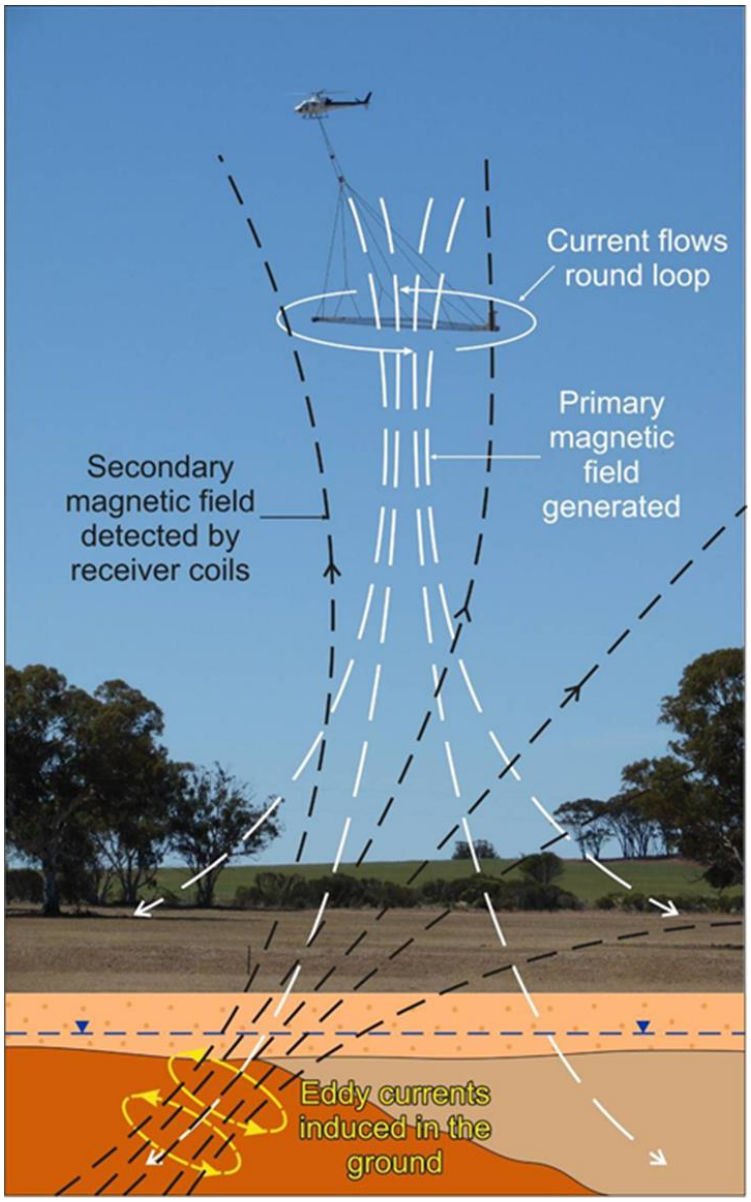

Figure 2-1: Operating principles of a helicopter airborne electromagnetic (AEM) system such as the SkyTEM system.

As the induced current results from the magnetic component of the electromagnetic field there is no need to have physical contact between transmitter or receiver and the ground. Consequently, EM surveys can proceed effectively both on the ground, and in the air.

The primary field travels from the transmitter to the receiver via paths above and below the ground surface (Figure 2-1). In the presence of a conducting body (for example conductive regolith and/or saline

groundwater), the magnetic component of the electromagnetic field penetrating the ground induces eddy, or alternating, currents to flow in the conductor. These eddy currents generate the secondary electromagnetic field which is measured by the receiver. In time domain EM systems, such as the SkyTEM AEM system, the receiver coils record the response of a decaying signal in the ground at various times (referred to as gates or time windows) after the transmitter pulse has been switched off.

The difference between the transmitted (primary) and received (secondary) electromagnetic fields will be determined by the geometry and electrical properties of conductors in the ground. Materials that are highly conductive produce strong secondary electromagnetic fields. Sediments (e.g. alluvium), soils or other regolith materials that contain saline pore water can generate such fields. The shape of the decaying signal provides information about the vertical conductivity structure of the ground.

Most AEM systems map contrasts in ground conductivity that are then interpreted based on experience and with the support of ancillary data, including surface and bore water EC, downhole conductivity measurements, lithology logs from drilling, surface geophysical investigations and other observations.

2.2 Limestone Coast SkyTEM survey extent

A SkyTEM^{312} airborne electromagnetic (AEM) survey was flown over an elongate survey area between the 30th September and 3rd October 2022. The survey area lies along the SA and VIC coast, 25km south of Mt Gambier, SA.

For this survey, a series of lines were flown orientated approximately perpendicular to the coastline, extending ~4.5km inland from the shoreline, with regular extended lines (~8km long) also being acquired. The survey area extended for ~60km along the coast, with a total of ~1,295.3 line-kilometres of data being acquired (including two repeat lines) (Figure 2-2). Line spacing varied along the extent of the survey The line spacing is variable across the area dependant on the project objectives in that zone.

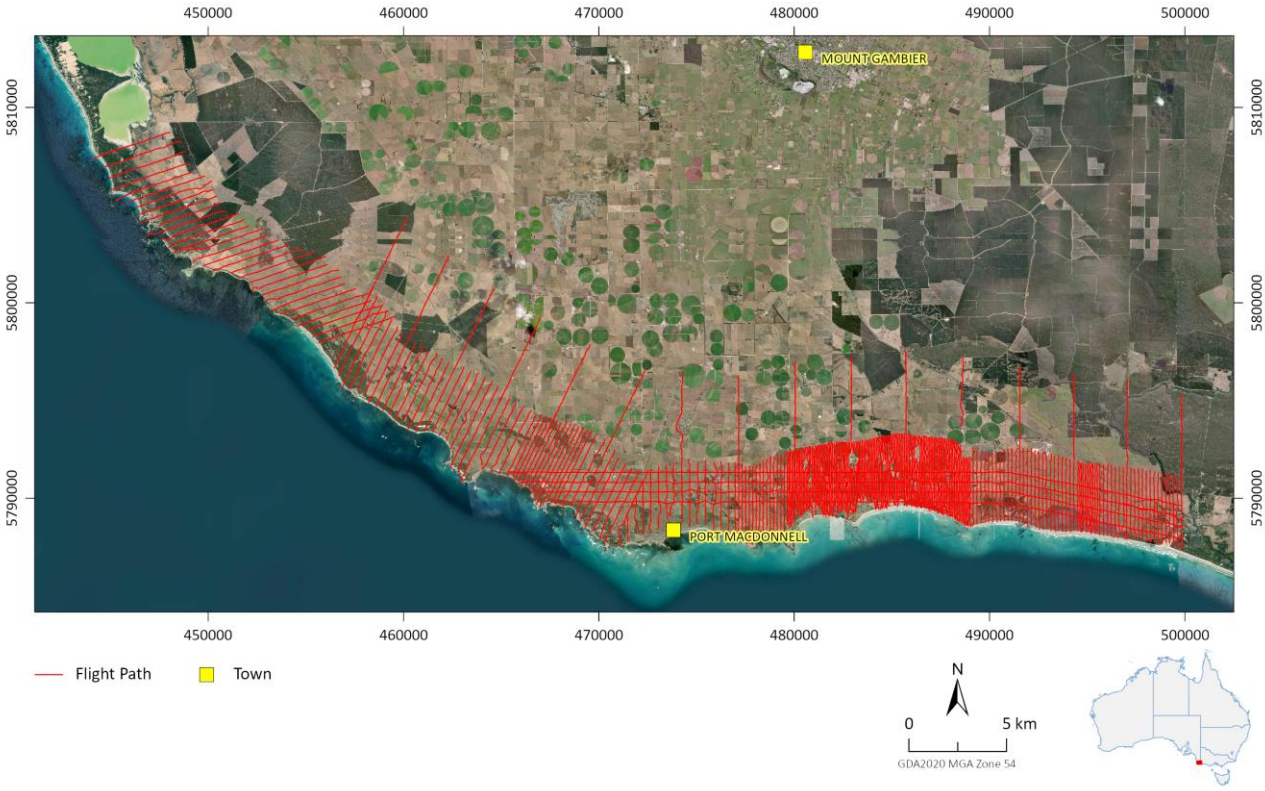

Figure 2-2: Airborne EM flight lines flown with the SkyTEM AEM system on the Limestone Coast

2.3 The SkyTEM AEM system

The SkyTEM system is a time domain helicopter-borne electromagnetic system developed in Denmark in 2004 (see Sørensen and Auken, 2004 for a more complete technical description). The system was originally developed for groundwater mapping purposes and in an Australian context it has been successfully applied to mapping of alluvial and sedimentary aquifers, and the saltwater interface in coastal regions (see, for example, Viezzoli et al. 2009; Brandes de Roo (2010); Lawrie et al. 2012; Davis et al. 2015, Gilgallon and McGivern 2018 and Munday et al. 2020).

The selection of the SkyTEM AEM system for this survey was predicated on the need to resolve near surface soil salinity variations, groundwater quality in the coastal sedimentary aquifers and the geometry of the saltwater interface (SWI) along the coast. Target depths were from surface to >100m. In addition to near surface resolution of the conductivity structure, there was also a need to define variations associated with deeper structures.

The SkyTEM EM system is carried as a sling load towed beneath a helicopter (Figure 2-3). For the Limestone Coast survey, the SkyTEM^{312} system was used. It has a six-sided transmitter loop mounted in a lightweight carbon-fibre frame with an area of 342 m^2 (SkyTEM 2022). The system operated in a dual transmitter mode, low moment (LM) and high moment (HM) and for the Limestone Coast survey all data was acquired using interleaved low and high moment transmitter modes with two different base frequencies (275Hz - low moment; 25Hz high moment, SkyTEM 2022) (see Table 2-1). The dual moment capability of the SkyTEM system provided the flexibility for shallow and deep sensing required for the study.

In the Low Moment mode, a low current, high base frequency and fast switch off provides early time data for shallow imaging. In contrast when in High Moment mode, a higher current and a lower base frequency provide late time data for deeper imaging. Peak current in the low moment is about 5.77 A; while the high moment transmits approximately 109.9 A (Table 2-1).

The receiver loop is rigidly mounted at the rear and slightly above the transmitter loop in a near-null position relative to the primary field, thereby minimizing distortions from the transmitter (see Figure 2-4). Additional details are provided in Tables 2-2 and 2-3 and in the acquisition and processing report (SkyTEM, 2022). Both X (inline) and Z (vertical) component data are recorded, but only the Z component data were used in the modelling of the Limestone Coast survey data.

The nominal survey altitude of the transmitter in the Limestone Coast survey was 45 – 60 m, with this varying depending on the presence of trees, power lines and related anthropogenic features. Data were pre-processed by filtering and then stacked data output every 0.5 s (~ 11 m on the ground) (SkyTEM 2022).

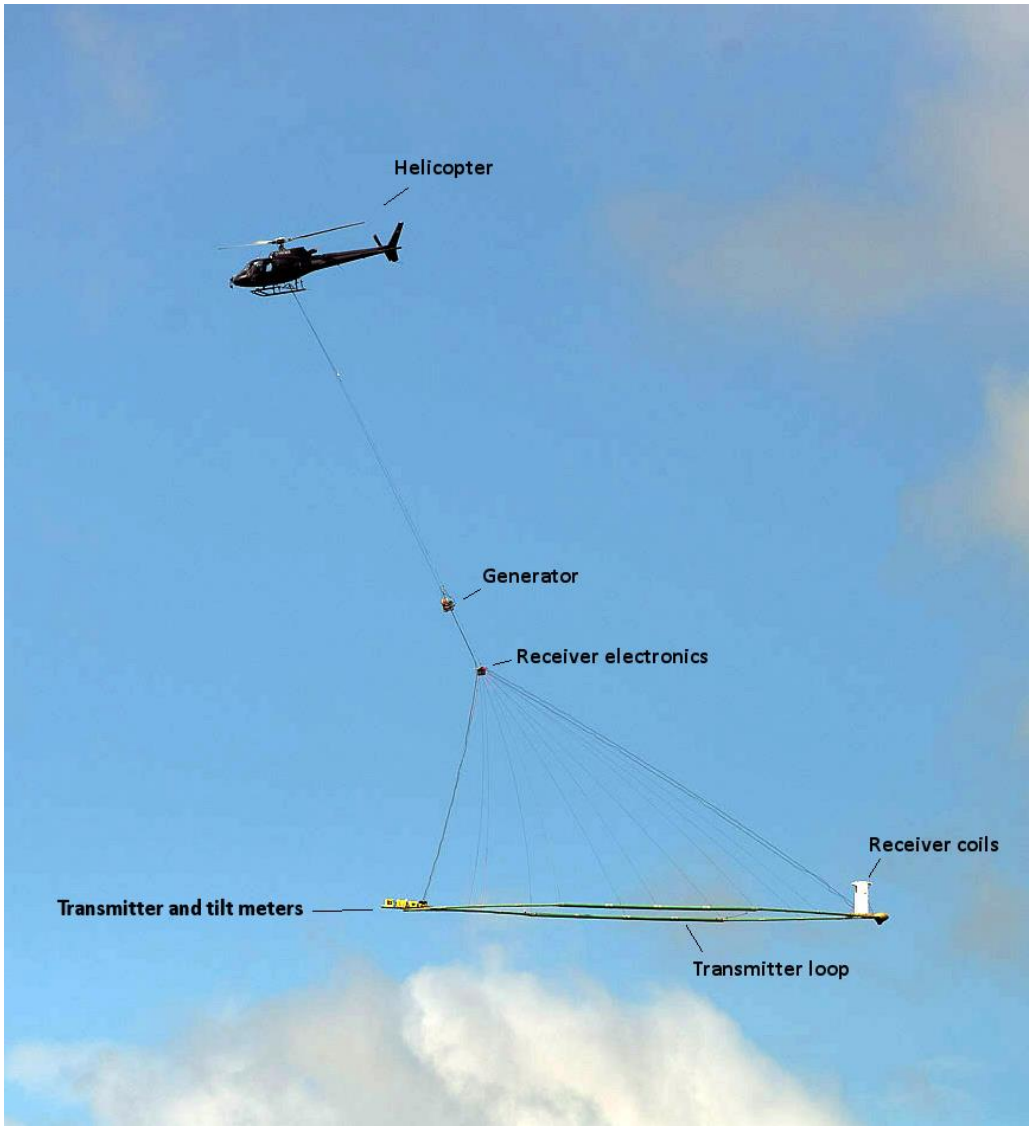

Figure 2-3: The SkyTEM^{312FAST} time domain airborne electromagnetic system in survey configuration.

Table 2-1: SkyTEM transmitter specifications.

EM TRANSMITTER	LOW MOMENT	HIGH MOMENT
Transmitter loop area	342m^2	342 m^2
Number of transmitter loop turns	2	12
Nominal peak current	5.77 A	109.9 A
Peak moment	4,036 Am^2	447,336 Am^2
Tx/Rx Frame height (nominal)	45-60m	45-60m m
Base frequency	275 Hz	25 Hz
Tx duty cycle	44%	25%
Tx waveform	Linear rise, linear ramp-off Bipolar	Pseudo-rectangular, linear ramp-off Bipolar
Tx on-time	0.8 ms	5 ms
Tx off time	1.018 ms	15 ms

Table 2-2: SkyTEM receiver specifications.

EM RECEIVER	LOW MOMENT	HIGH MOMENT
EM Sensors	dB/dt coils	dB/dt coils
Rx coil effective area (Z and X)	325 m^2 (Z)/115.5 m^2 (X)	325 m^2 (Z)/115.5 m^2 (X)
Low pass cut-off frequency for Rx coils	206.8kHz (Z) 348.3kHz (X)	206.8kHz (Z) 348.3kHz (X)
Low pass cut-off frequency for Rx electronics	300 kHz	300kHz
Front gate	0.00 µs	370.0 µs
Earliest gate centre time Measured/recommended use	16.415 µs (Gate 9)	436.415 µs (Gate 16)
Latest gate centre time	861.415 µs (LM) Gate 26	13187.415 µs (HM) Gate 38

Table 2-3: Position of receiver.

Z-COMPONENT R_X COIL POSITION	
Behind Tx loop centre	13.3 m
Above plane of Tx loop	2.00 m
X-COMPONENT R_X COIL POSITION	
Behind Tx loop centre	14.65 m
Above plane of Tx loop	0 m

Tables 2-4 and 2-5 show the time windows (also referred to as channels or gates) for the low and high moment for the Limestone Coast SkyTEM survey. These gate times have had a time shift applied to them according to the calibration factors relevant to the AEM system used for the survey (see SkyTEM, 2022).

Table 2-4: SkyTEM312 Low Moment gate times. All gate times are relative to the start of the transmitter current ramp down Gate times for Low Moment (Source SkyTEM 2022).

LM GATE NUMBER	GATE WIDTH (µs)	GATE OPEN (µs)	GATE CENTRE (µs)	GATE CLOSE (µs)
9	3.57	14.63	16.415	18.2
10	4.57	18.63	20.915	23.2
11	5.57	23.63	26.415	29.2
12	7.57	29.63	33.415	37.2
13	9.57	37.63	42.415	47.2
14	12.57	47.63	53.915	60.2
15	15.57	60.63	68.415	76.2
16	19.57	76.63	86.415	96.2
17	24.57	96.63	108.915	121.2
18	30.57	121.63	136.915	152.2
19	50.57	152.63	177.415	203.2
20	50.57	203.63	228.915	254.2
21	50.57	254.63	279.915	305.2
22	100.57	305.63	355.915	406.2
23	100.57	406.63	456.915	507.2
24	100.57	507.63	557.915	608.2
25	151.57	608.63	684.915	760.2
26	201.57	760.63	861.415	962.2

Table 2-5: SkyTEM312 High Moment gate times. All gate times are relative to the start of the transmitter current ramp down (Source SkyTEM 2022).

LM GATE NUMBER	GATE WIDTH (μs)	GATE OPEN (μs)	GATE CENTRE (μs)	GATE CLOSE (μs)
16	19.57	426.63	436.415	446.20
17	24.57	446.63	458.915	471.20
18	30.57	471.63	486.915	502.20
19	50.57	502.63	527.415	553.20
20	50.57	553.63	578.915	604.20
21	50.57	604.63	629.915	655.20
22	100.57	655.63	705.915	756.20
23	100.57	756.63	806.915	857.20
24	100.57	857.63	907.915	958.20
25	151.57	958.63	1034.915	1110.20
26	201.57	1110.63	1211.415	1312.20
27	252.57	1312.63	1438.915	1565.20
28	353.57	1565.63	1742.415	1919.20
29	403.57	1919.63	2121.415	2323.20
30	504.57	2323.63	2575.915	2828.20
31	707.57	2828.63	3182.415	3536.20
32	807.57	3536.63	3940.415	4344.20
33	1009.57	4344.63	4849.415	5354.20
34	1211.57	5354.63	5960.915	6566.20
35	1415.57	6566.63	7274.415	7982.20
36	1819.57	7982.63	8892.415	9802.20
37	2019.57	9802.63	10812.415	11822.20
38	2729.57	11822.63	13187.415	14552.20

The two moments provide the means to resolve near surface conductivity variability as well as deeper changes in the ground conductivity structure as mentioned previously.

The SkyTEM system is calibrated (Foged et al., 2013), in the laboratory, and verified at the Danish National Reference Site (GeoFysikSamarbejdet, Aarhus University, 2012). Consequently, the data set acquired by the system in the study area did not necessarily require the acquisition of additional ground calibration data or the use of external calibration procedures to ensure the generation of accurate models of ground conductivity. This is discussed further in later sections.

2.4 AEM System Spatial Resolution

The spatial resolution and depth of investigation of an AEM system varies with the system type, flight height and ground speed, power, sample time and/or frequency, and ground conductivity (Reid et al., 2006, Spies & Woodgate, 2005). Resolution of variations in electrical conductivity differs in the horizontal and vertical direction. Commonly the system spatial resolution is considered in terms of the volume of the ground that contributes most of the response for each sounding or measurement.

Helicopter systems such as SkyTEM return a weighted average response over lateral distances of up to 100 metres or more, dependent upon flying height, transmitter loop size, speed of data acquisition, and the sampling rate of the system. Even though survey data may be provided at spatial rates of 15-25 m per sample, the smallest lateral (horizontally orientated) features that can be resolved near surface are around 30-60m

for helicopter systems where good conductivity contrasts are present. Resolution of horizontal features will deteriorate with increasing depth below the surface. Resolution along the line is governed by the sampling rate of the system, which may vary between different AEM systems, but it is also affected by the proprietary processing by the airborne contractor, who may use filtering methods on the data acquired to reduce the effect of noise. The implication of the above discussion is that measurements along a flight line are often on the order of a few tens of metres. An indication of the sampling volume for the helicopter AEM systems compared with ground and fixed wing EM systems is summarised in Figure 2-4.

Commonly the system spatial resolution is considered in terms of the volume of the ground that contributes most of the response for each sounding or measurement. Normally the highest resolution is measured along a flight line, with the perpendicular resolution being determined, in part by flight-line spacing. These issues should be borne in mind when comparing models derived from the AEM data to ground conductivity or other products collected from ground and borehole surveys, or individual soil pits, where the spatial resolution is usually sub-metre in dimension.

In conductive terrains low flying systems are better able to penetrate the conductive overburden (Macnae, 2007).

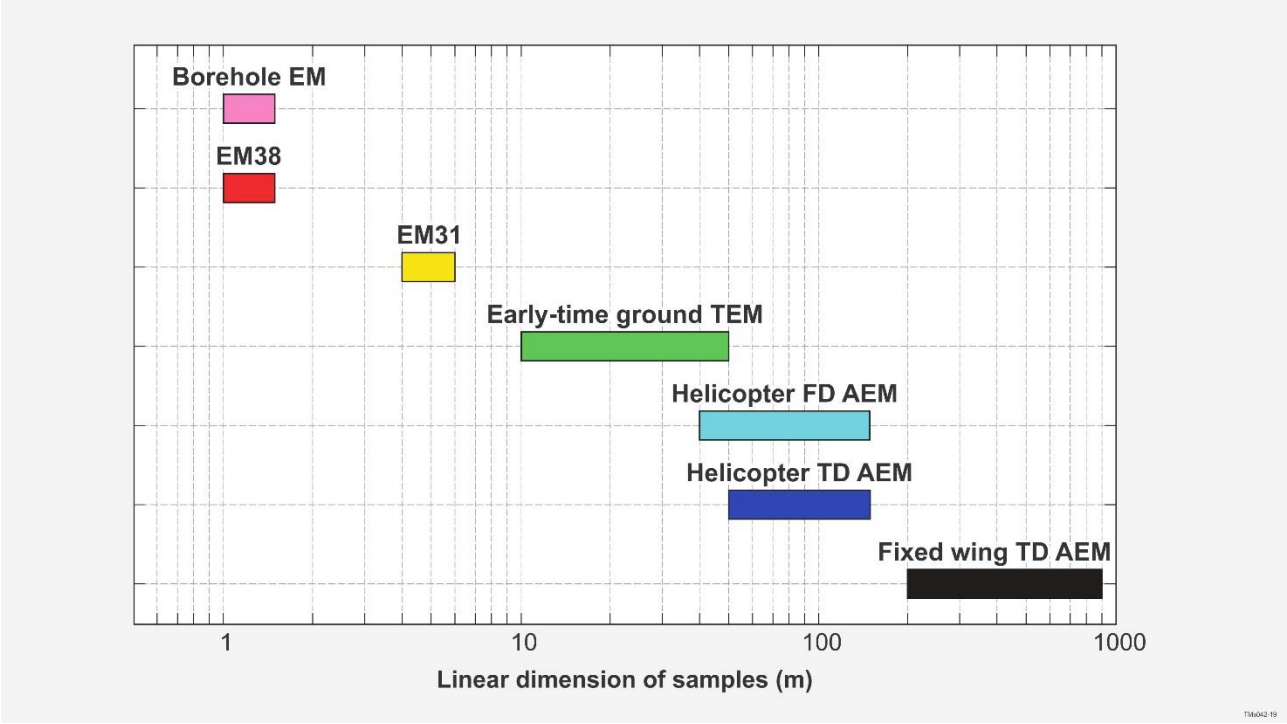

Figure 2-4: Linear scale of lateral averaging as an indicator of sampling volume for a range of ground and airborne EM systems; including borehole, ground surface and airborne systems. Data from a helicopter TD (time domain) AEM system is considered in this report (adapted from figure by R. Lane, Geoscience Australia).

3 Subsurface Conductivity Structure

3.1 Factors affecting ground conductivity

The measured electrical conductivity (the reciprocal of resistivity) of the regolith and overlying sediments is a measure of how easily an electrical current can pass through them. Conductivity itself is a complex function of a number of variables including:

- concentration of dissolved electrolytes - the concentration of ionic conductors in solution;
- amount and composition of clays - particularly those with a moderate to high cation exchange capacity (CEC);
- moisture content - the extent to which the pores are filled by water;
- porosity: shape and size of pores, number, size and shape of interconnecting passages; and
- temperature.

Sedimentary rocks, whether consolidated or unconsolidated are characterised by a range of conductivities (Figure 3-1), but the influence of contained water quality and quantity can also be significant (Palacky 1983, 1987). It is reasonable to assume that the observed ground conductivity, whether measured by a ground or airborne system, would be non-unique for any given lithology. In both consolidated and unconsolidated regolith and sedimentary materials, including alluvial materials and underlying basement rocks, the conductivity will be significantly influenced by the electrolyte (salt) which occurs in moisture-filled pores within an insulating matrix (McNeill 1980, 1990).

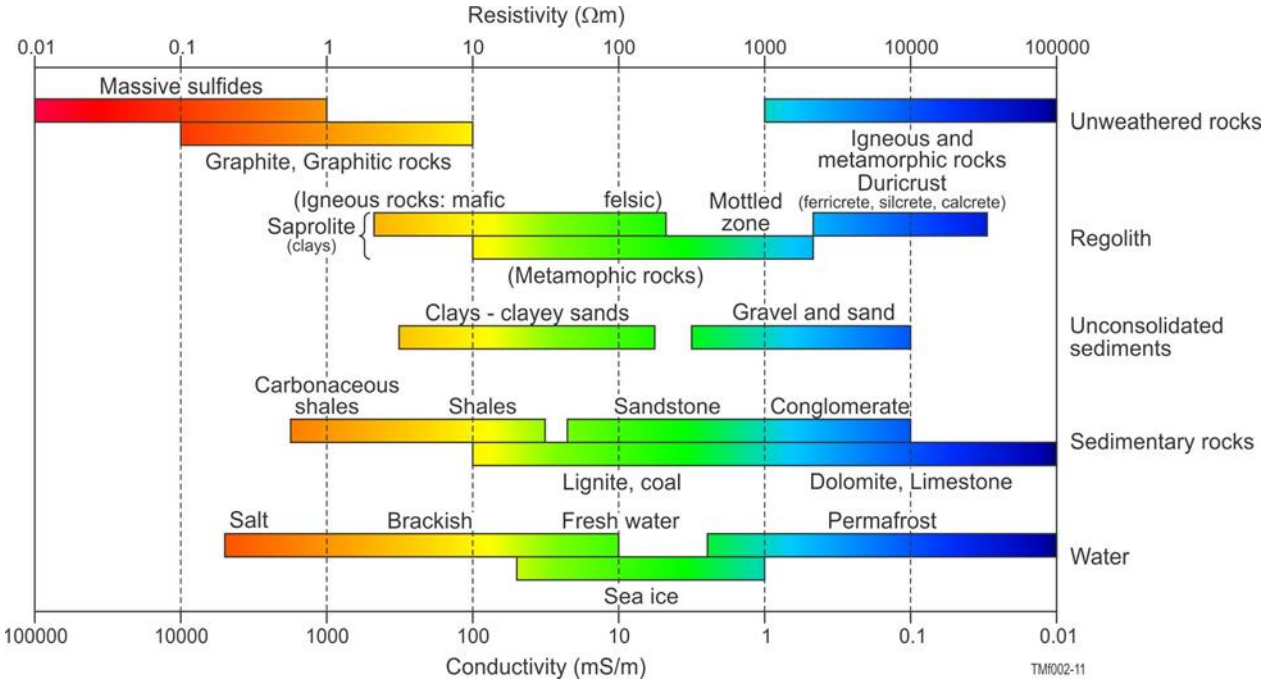

Figure 3-1: Schematic indicating some of the electrical properties of sediments, regolith materials and water. The overlapping responses indicate that the observed ground conductivity defined by an airborne EM system are likely to be non-unique (adapted from Palacky 1983). Conductivities are specified in mS/m.

In unweathered basement rocks, resistivities are likely to be very high (see Figure 3-1), and consequently you might expect a sharp contrast between an “electrolyte-rich” regolith or sediment, versus a basement that is likely to be “electrolyte-poor”. Whilst the porosity and connectivity of the pores in sediments and in-situ

regolith materials play a part in driving conductivity, particularly in the absence of clays, it is the quantity and in particular the quality of the contained pore water that is critical. Clay content and type become important when the concentration of ionic conductors (for, example, salts in solution) is low. Their significance becomes negligible at high ionic concentrations, particularly for clays of low to moderate CEC (cation exchange capacity) such as kaolinite (Emerson and Yang, 1997).

Given the variable quality of groundwater contained in the sedimentary sequences along the Limestone Coast, it is reasonable to expect that the modelled conductivity structure for SkyTEM data set will *primarily* reflect variations in water quality associated with particular stratigraphic units, but factors linked to lithology-type and texture (i.e. grain size, porosity and grain orientation) are also likely to play a role. However, a relationship between sediment type and salinity can occur. In some instances, transported silts and clays may often contain more saline groundwater, than coarser textured units. In these circumstances, an association between material type and conductivity can be inferred. Clay-rich sedimentary units may sometimes contain saline groundwater, partly influenced by the slow movement of water through them, encouraging the accumulation of salts in their pores.

3.2 AEM data inversion – The derivation of ground conductivity

Given that one of the primary objectives of the Limestone Coast survey was to map and interpret spatial variations in conductivity it was necessary to convert measurements of the electromagnetic response to ground conductivity and present the results in a form that allow their ready analysis against existing or new ground data. This is achieved through a modelling process known as inversion.

The inversion of AEM data and their presentation as maps or sections detailing a conductivity distribution in the subsurface is now commonplace. The representation of continuous and gradational conductivity distributions as discrete conductive “units” or bounding layers is an effective way of summarising information from large AEM surveys. It enables users to visualise conductivity variations in the subsurface in three dimensions (Lane 2000, 2002, Lane and Pracilio, 2000). To determine true conductivity variation with depth the data must be modeled. This entails taking data from each measurement point, sounding or fiducial along a flight line and estimating the parameters of a layered-earth, conductivity-depth model, which would produce the observed response (Figure 3-2). Through the application of approximate transforms or layered inversions, conductivity values with depth can be calculated for each observation (sounding) made by the AEM system and then stitched together into sections to provide a representation of the 2D variation of conductivity. This is sometimes referred to as a “para-section” or “stitched-section”. Further, the conductivity depth profiles can be combined into a 3D gridded volume from which arbitrary sections, horizontal depth slices (or interval conductivity images) and iso-surfaces can be derived. In this study, depth slices were extracted from the inversion results and then gridded as a 2D maps of conductivity for a given depth interval. The schematic in Figure 3-2 summarises the process of acquiring AEM data, inverting the resulting data, and presenting the results as conductivity images.

Airborne electromagnetic (AEM) data acquired for exploration or environmental applications are commonly modelled using algorithms such as conductivity depth transforms (CDT’s) or Layered Earth Inversions (LEI’s) that assume a 1D earth (Sattel 1998, 2005). Presently, the application and relevance of full 2 or 3D inversion of AEM data remains undetermined, although more recent case studies (see, for example, Paterson et al. 2016) are providing greater insight into their application. In many respects it may be unrealistic and unnecessary to employ these computationally intensive methods particularly for the investigation of sedimentary sequences in many Australian settings, where it is reasonable to assume that the subsurface, *at the scale of the footprint of an AEM system,* can be represented as a series of horizontal layers. The 1D model assumption, legitimate in sub-horizontal, layered sedimentary areas where it produces results that are only slightly distorted by 2D or 3D effects which may be induced by faults, fractures, or other geological phenomena (Auken et al., 2005; Newman et al., 1987; Sengpiel and Siemon, 2000).

In the following section we explore the processing and inversion methods used to interpret the Limestone Coast data set.

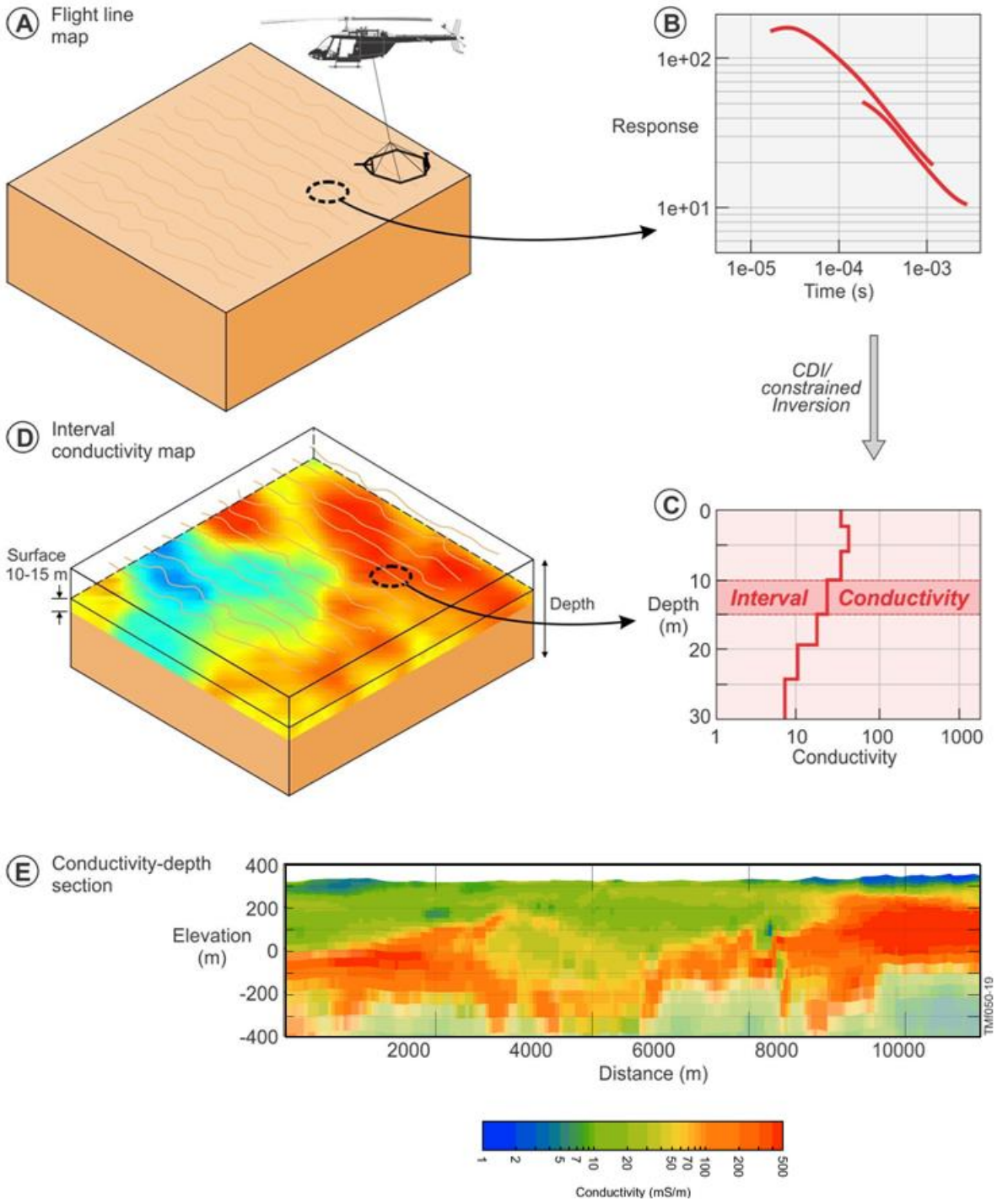

Figure 3-2: Schematic representation of SkyTEM helicopter time domain EM data acquisition and interpretation. A) Data are acquired along parallel flight lines, with high and low moment data recorded at fixed time intervals (soundings) along each flight line; B) The EM receiver located behind and offset from the transmitter towed beneath the helicopter measures the secondary high and low moment responses; C) The measured response is used to determine the conductivity-depth function by transformation or inversion. Conductivity-depth values can be calculated for each observation, taking account of the elevation of the system above the ground; D) The modelled conductivity structure for each sounding can then gridded into conductivity-depth intervals to provide a spatial representation of the subsurface conductivity structure at different depths below the ground surface. These maps can be shown as elevations (mAHD) or as depth intervals below the ground surface ground surface; E) Individual soundings from a flight line or transect of several soundings may also be stitched together into conductivity-depth sections to provide a representation of the 2D variation of conductivity, sometimes referred to as a "para-section", or "stitched section".

4 Data Processing and Inversion

4.1 Introduction

In this section, we describe the processing and inversion steps taken to convert the AEM data into models of electrical conductivity in the subsurface. These steps were taken to ensure that the quality of the data input into the inversion algorithm was described correctly with a robust noise estimate for the survey. As a first step, we removed all data in the survey where the transmitter altitude was greater than 80 m. There were only a few points in the survey that needed to be culled due to altitude. In the second step of the processing, we subsampled the survey line to 25 m station intervals. This was done to reduce the overall computational burden for the inversions. A station interval of 25 m was chosen based on the survey flight line spacing and the grid cell size resolution expected for the final gridded products. Finally, we implemented a novel technique for estimating noise in the AEM survey based on 1D reversible-jump Markov chain Monte Carlo estimations (RJMCMC). The method employed is summarised in the following subsection.

4.2 Reversible-jump Markov chain Monte Carlo estimation of AEM noise

Inversion of AEM data for electrical conductivity models involves many factors that need to be addressed. These include: the description of the AEM system to be modelled, discretisation of the model used to estimate conductivity, the choice of inversion algorithm, and the amount of regularisation needed to ensure reasonable convergence. Perhaps one of the most important factors that needs to be mentioned, and one that is closely tied to model regularisation, is estimates of noise in the AEM survey data. Noise is any unwanted signal that interferes with the electromagnetic signal transmitted and received by the AEM sensor. It can be generated by various sources categorised as anthropogenic or natural. The former comprises man-made structures such as buildings, pipelines, fences and power lines, with the latter including sferics (a broadband electromagnetic impulse resulting from natural atmospheric lightning discharge) and other atmospheric disturbances. Other natural noise sources include variations in the earth's natural electromagnetic fields and, one that is rarely discussed, the actual geological variability of the survey area.

Different types of noise can be present in AEM data, but they are generally classified as random and systematic noise. Systematic noise, caused by a specific source that produces a consistent pattern of interference in the AEM data, can often be corrected by identifying the source and applying appropriate correction methods. Random noise is caused by the statistical variation of the electromagnetic signal received by the AEM sensor. This noise is difficult to remove as it is not correlated with any causes.

An accurate estimation of noise levels in AEM survey data is considered necessary since they directly influence the accuracy and reliability of the data and the models of the subsurface conductivity structure, that can be generated from them. This can have a profound impact on our interpretation of the subsurface geology. Despite the importance of obtaining accurate estimates of data noise, there is relatively little in the literature that describes how we obtain them.

It can be difficult to determine the noise characteristics of AEM survey data since there is little opportunity to operate AEM systems at full capacity while on the ground. To address this, many contractors now offer measurements of high-altitude data. With the transmitter operating at full capacity, the AEM system is taken to extreme altitude in the assumption that the signals measured by the receiver coils will be uninterrupted or affected by earth responses. These measurements offer an understanding of the noise floor of the AEM receiver assembly: the measurements of the receivers in the absence of any signal other than the system itself. This is a good first step to understanding the bias of the system. An example of high-altitude noise recordings is shown with the solid lines in Figure 4-1.

Green and Lane (2003) suggest a different strategy for estimating noise in survey data through use of repeat lines. The assumption here is that the system should always measure the same responses over the same survey transect. They recommend characterising noise as either additive or multiplicative in nature, meaning that noise levels for a given delay time are composed of some base level of noise plus some factor multiplied by the signal itself at that delay time. This can be written as

$$\sigma_i = \sqrt{\sigma_{iadd}^2 + (\sigma_{im} \cdot d_i)^2}, \quad (1)$$

where σ_i is the noise at delay time i, d_i is the measured data for that delay time, and σ_{iadd} and σ_{im} are the additive noise term and the multiplicative factor, respectively. It should be noticed that the noise term σ_i enters the data misfit equations as an additive term when used in this manner. An example of an additive noise estimate following this method is shown with dashed lines in in Figure 4-1.

One of the drawbacks of the method of Green and Lane (2003) is that repeat lines are impossible to replicate exactly due to the platforms being airborne. Differences in altitude can have a profound effect on the measured response. Another drawback is that many older surveys do not have repeat lines flown (or are not available as part of the delivered data); so, a compromise must be sought. In the approach taken here, we assume that while repeat lines may not have the same measured responses due to variations in acquisition, they should have the same earth and noise model provided the repeat lines are flown reasonably close together. At each station of the repeat lines, differences between the recorded data and the forward response for each station can therefore be classified as 'noise'. Noise in this sense incorporates variations in measurement at each station but also encompasses the choice of model used to determine the earth response.

To achieve estimates of electrical conductivity distribution and noise for the repeat lines, we employ the Reversible-jump Markov chain Monte Carlo (RJMCMC) method described by Green, (1995) with a few modifications similar to those employed by Minsley et al., (2021).

We begin by ensuring that sampling of the repeat line data is consistent across a regular spacing along the survey line. The simplest way of doing this is by taking stations from each repeat line that are close enough that we can assume they are measuring the same volume of the earth (eg, Reid et al., 2006) or by resampling the data to a regular spacing. For every station, we create a 1D layered-earth model of variable electrical conductivity layers (and thickness) and a common noise estimate for every delay time of the system. Using $\boldsymbol{m_s}$ to describe the model at station s, the model is composed of k layers of resistivity $\boldsymbol{\rho}$ with thickness $\boldsymbol{t}$ to describe the earth, and n values of $\boldsymbol{\sigma}$ to describe the additive error applied to the n delay times for the j measurements at location s. Notice that the variables in bold are vectors.

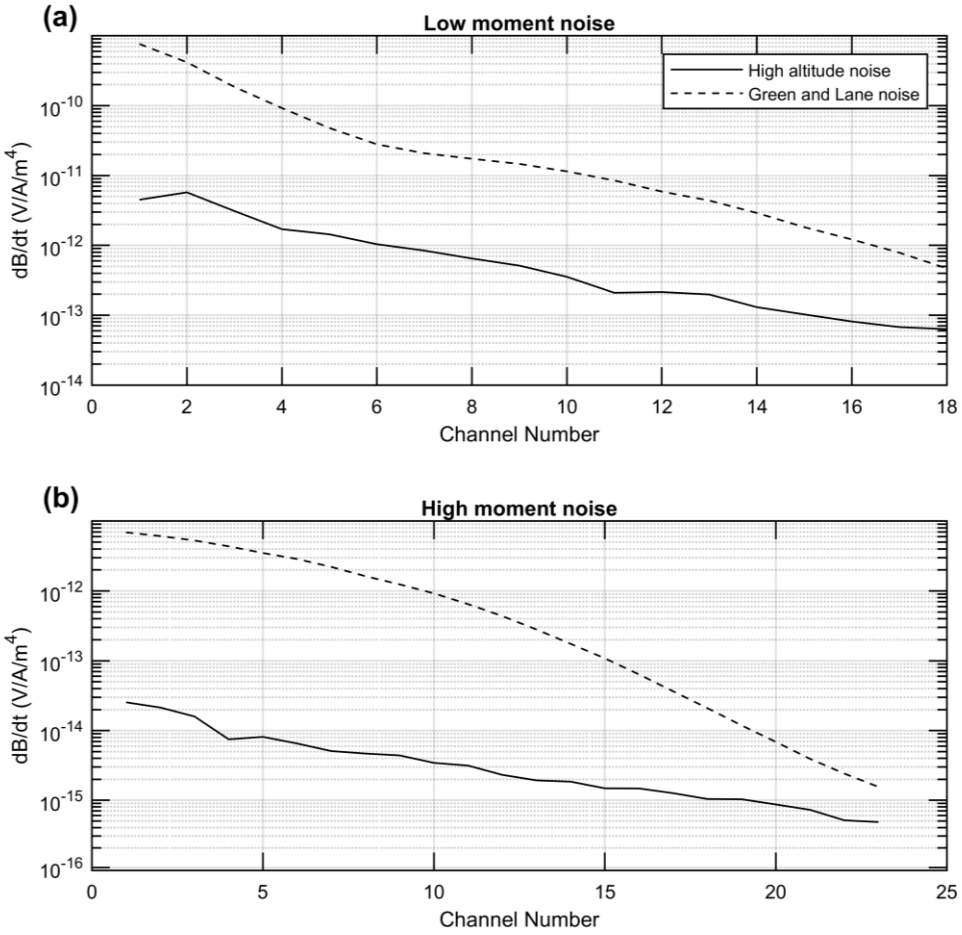

Figure 4-1: Noise estimates from an AEM system. Solid black lines show the high-altitude measurements, while the dashed lines show the estimates from a Green and Lane (2003) analysis of repeat lines.

At every iteration in the chain, a new model $\boldsymbol{m'_s}$ is proposed from the previous model $\boldsymbol{m_s}$. The new model is accepted or rejected based on the Metropolis, Hastings, Green (MHG) algorithm according to the following acceptance criterion α

$$\alpha(\mathbf{m'_s}|\mathbf{m_s}) = \min\left[1, \frac{p(\boldsymbol{m'_s})}{p(\boldsymbol{m_s})}\frac{p(\mathbf{d}|\boldsymbol{m'_s})}{p(\mathbf{d}|\boldsymbol{m_s})}\frac{q(\boldsymbol{m_s}|\boldsymbol{m'}_s)}{q(\boldsymbol{m'}_s|\boldsymbol{m_s}),}|\mathbf{J}|\right], \tag{2}$$

where $p(\boldsymbol{m'_s})/p(\boldsymbol{m_s})$ is the prior ratio of the models, $p(\mathbf{d}|\boldsymbol{m'_s})/p(\mathbf{d}|\boldsymbol{m_s})$ is the likelihood ratio of the data given the models, $q(\boldsymbol{m_s}|\boldsymbol{m'}_s)\backslash q(\boldsymbol{m'}_s|\boldsymbol{m_s})$ is the proposal ratio, and $\boldsymbol{J}$ is the Jacobian governing changes between dimensions. Of special interest is the data likelihood function $p(\mathbf{d}|\boldsymbol{m_s})$ which will change at every iteration due to choices of perturbations in k, $\boldsymbol{\rho}$, $\boldsymbol{t}$, or $\boldsymbol{\sigma}$. We write the likelihood function as

$$p(\mathbf{d}|\boldsymbol{m_s}) = \sum_{i=1}^{j}\frac{1}{\sqrt{2\pi|\boldsymbol{C_d}(\boldsymbol{\sigma})|}}\exp\left(-\frac{1}{2}\left((\boldsymbol{f}(\boldsymbol{\rho},\boldsymbol{t},k)-\boldsymbol{d_{si}})^T\boldsymbol{C_d}(\boldsymbol{\sigma})(\boldsymbol{f}(\boldsymbol{\rho},\boldsymbol{t},k)-\boldsymbol{d_{si}})\right)\right) \tag{3}$$

where $\boldsymbol{f}(\boldsymbol{\rho},\boldsymbol{t},k)$ is the predicted data given the model parameters, $\boldsymbol{d_{si}}$ is the measured data at station s for measurement i ,and $\boldsymbol{C_d}(\boldsymbol{\sigma})$ the data covariance matrix that models the error in the system responsible for the measurements. In this report, $\boldsymbol{C_d}(\boldsymbol{\sigma})$ is assumed to be diagonal.

Model proposals are based on the usual choices for MHG samplers. At every iteration, we choose to: create a conductivity interface, destroy a conductivity interface, change the structure of the existing model (by creating and destroying random interfaces, or vice versa), or changing one of the n noise parameters in $\boldsymbol{\sigma}$. For each station, several chains (8) are run for many iterations (3×10^5). Several thousand models are excluded from the beginning of each of the chains, and the results are accumulated.

A posterior mean electrical conductivity distribution transect for the example discussed earlier is shown in Figure 4-2. Areas that are made transparent reveal that the spread in conductivity of the accepted models is almost equivalent to the prior probability range of the conductivity proposals (and, therefore, less informative). The section looks reasonable, and there is clear structure to depths of approximately -400 mAHD. Figure 4-3 shows the mean distributions of the marginalised noise estimates for every model in the reduced RJMCMC chains, and for every station. The distributions are shown in shaded blue, while the mean additive noise value for each delay time is marked by the solid gold line. The mean values from the gold line are chosen to represent the average additive noise values for the entire survey. Also shown are the high-altitude (black), and the Green and Lane (2003) noise estimates (red). The RJMCMC noise estimates are consistently higher than the high-altitude noise estimates, but mostly lower than the Green and Lane (2003) estimates. For the remainder of this report, we use the RJMCMC estimates of noise in the models for estimating electrical conductivity.

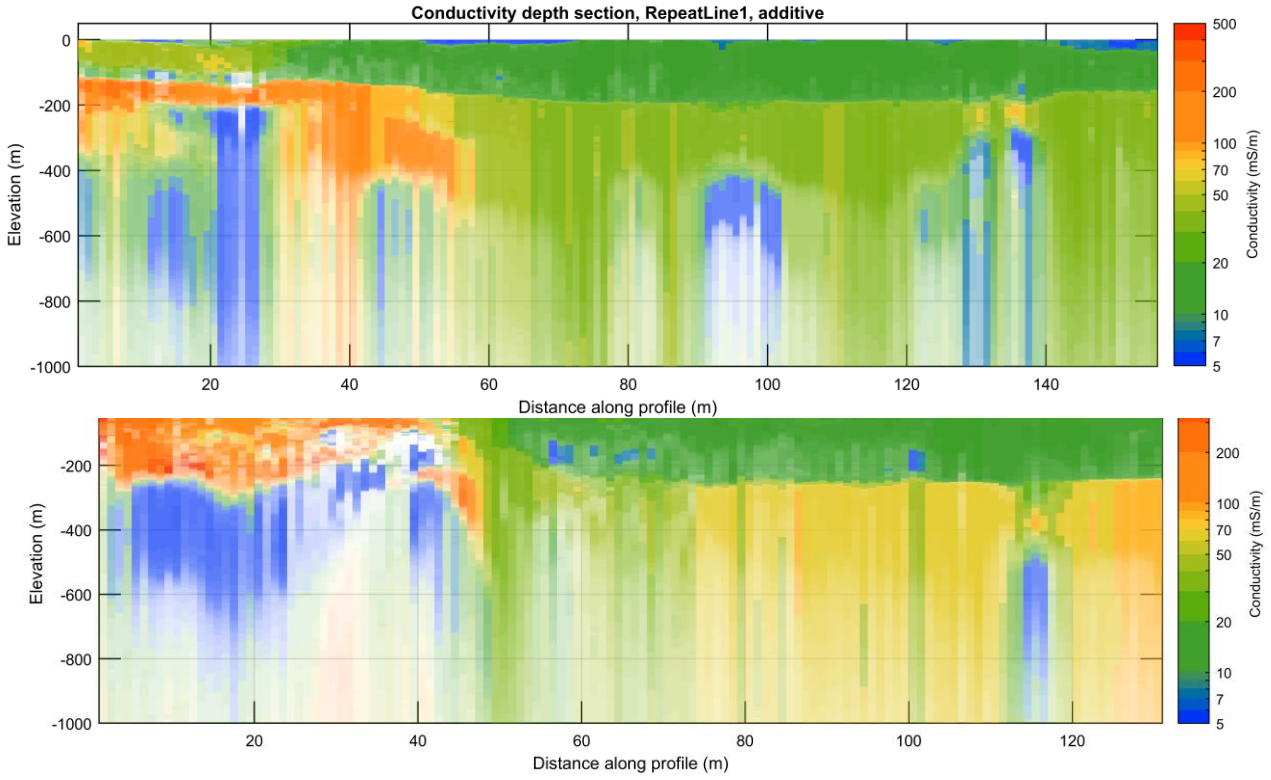

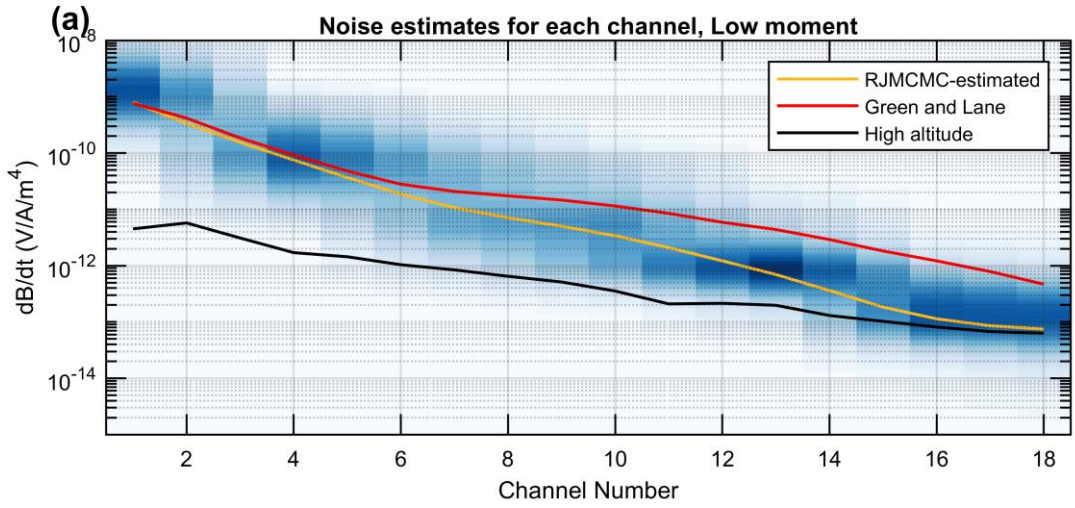

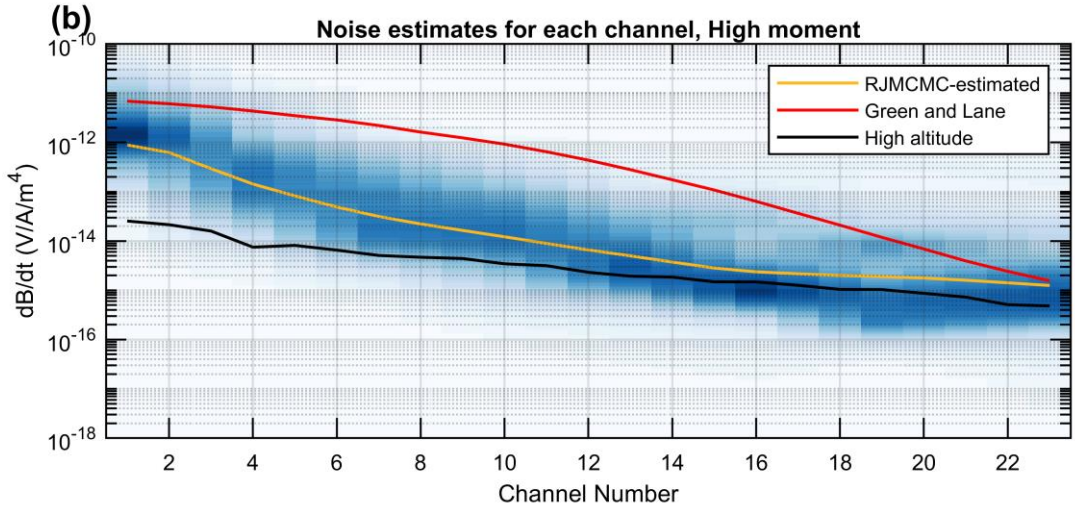

4.3 Description of the inversion algorithm

Having determined an average noise estimate for the entire survey based on several repeat lines, it is useful to see the effect the noise estimates have on deterministic inversion. The deterministic inversion algorithm is run by trying to minimise an objective function that compares the data measured while on survey to the data predicted by the layered earth forward model.

Briefly, the objective measure function ϕ can be written

$$\phi = (\boldsymbol{f}(\boldsymbol{m}) - \boldsymbol{d})^{\boldsymbol{T}} \boldsymbol{C_d^{-1}} (\boldsymbol{f}(\boldsymbol{m}) - \boldsymbol{d}) + \alpha (\boldsymbol{m} - \boldsymbol{m_p})^{T} \boldsymbol{C_m^{-1}} (\boldsymbol{m} - \boldsymbol{m_p}), \quad (4)$$

where $\boldsymbol{f}(\boldsymbol{m})$ is the predicted data at a survey location based on a layered earth conductivity model $\boldsymbol{m}$, $\boldsymbol{d}$ is the data measured at the survey locations, $\boldsymbol{C_d}$ is the data covariance matrix, $\boldsymbol{m_p}$ is the prior layered earth electrical conductivity model, $\boldsymbol{C_m}$ is the model covariance matrix that determines the smoothness in the

model structure, and α is the model smoothness factor that governs the influence of the smoothness and the prior model in the objective function. Figure 4-4:

Equation (4) describes the objective function to be minimised in the inversion algorithm that models electrical conductivity of the subsurface resulting from measurements of electromagnetic survey data in the region of interest. The first term is a comparison of the predicted data for a given model to the data measured by the system, weighted by the noise in the data. We call this term the model misfit. Because the difference between measured and predicted data is added together in a squared sense, the model misfit measure can be described as an L_2 norm. The second term, also L_2, is the model misfit. It is a comparison between the updated electrical conductivity model and the prior electrical conductivity model. The factor $(\boldsymbol{m} - \boldsymbol{m_p})$ is weighted by the inverse of the model covariance matrix ($\boldsymbol{C_m^{-1}}$), otherwise known as the precision matrix. The precision matrix imposes restrictions on the model parameters themselves and the relationship between adjacent and nearby model parameters. For example, the second term in Equation (4) penalises large differences between model parameters. It behaves, therefore, as a smoothing operator. The factor α modifies the importance of the model misfit term in the objective function. Our goal is to achieve a model that is smooth enough to satisfy the model misfit term, yet rough enough to satisfy the data misfit term.

The inversion of the survey data to electrical conductivity models is non-linear, ill-posed and often ill-conditioned. This means that the forward model prediction $\boldsymbol{f}(\boldsymbol{m})$ can vary greatly depending on input parameters and that there are infinitely many model parameter combinations that can satisfy the misfit function. We conduct the inversion solution, despite the ill-posedness of the problem and the poor conditioning of the matrices, using iterative methods. Beginning with a starting model of the electrical conductivity of the subsurface, we compute the sensitivity of the predicted data to the model parameters and the data and model misfits. Using the sensitivity matrix and the misfit values, we update the model parameters using a linear approximation to the perturbation of the objective function resulting from varying the model parameters. We stabilise the linear approximation by using the Levenberg-Marquardt (LM) method (Levenberg 1944; Marquardt 1963) to provide model updates. Updates to the LM parameter are based on the work of Zhao and Fan (2016).

4.4 Effect on Regularisation

Figure 4-4 shows smooth 1D layered earth inversion models for a wide range of model regularisation values of α on repeat line 1 from this survey. In these inversions, an isotropic exponential model with 25 m correlation length was chosen for the model regularisation and only the weighting was changed. The prior resistivity was chosen to be a 10^4 Ωm half space. A depth of investigation line (DOI) (Christiansen and Auken 2012) for each inversion is shown in white. The figures show little variation in inverted conductivity models above the DOI line, as is more clearly illustrated in Figure 4-5. This indicates that the model regularisation has little effect in determining model structure where the models are informed by the data, which is precisely what is desired in an inversion.

In addition to Figure 4-4 and Figure 4-5, it is also useful to visualise the trade-off between data misfit and model misfit for different values of α. One convenient way to demonstrate this is the use of an L-curve (Hansen 1998), as shown in Figure 4-6. This figure shows how data misfit reduces – and model misfit increases – with decreasing regularisation. We generally take the point of maximum curvature in the L-curve for the optimum choice of model regularisation, but this can be an arbitrary choice. In this report, we have chosen an α value of 0.215 for all inversions as it yields models that closely resemble the results from the RJMCMC estimations. A comparison of the inverted model using α = 0.215 and the RJMCMC model for repeat line 1 is shown in Figure 4-7. We can see that much of the fine structure of the RJMCMC inversion is faithfully recovered in the inverted model at a fraction of the total computational cost. A comparison plot for repeat line 2 is shown in Figure 4-8

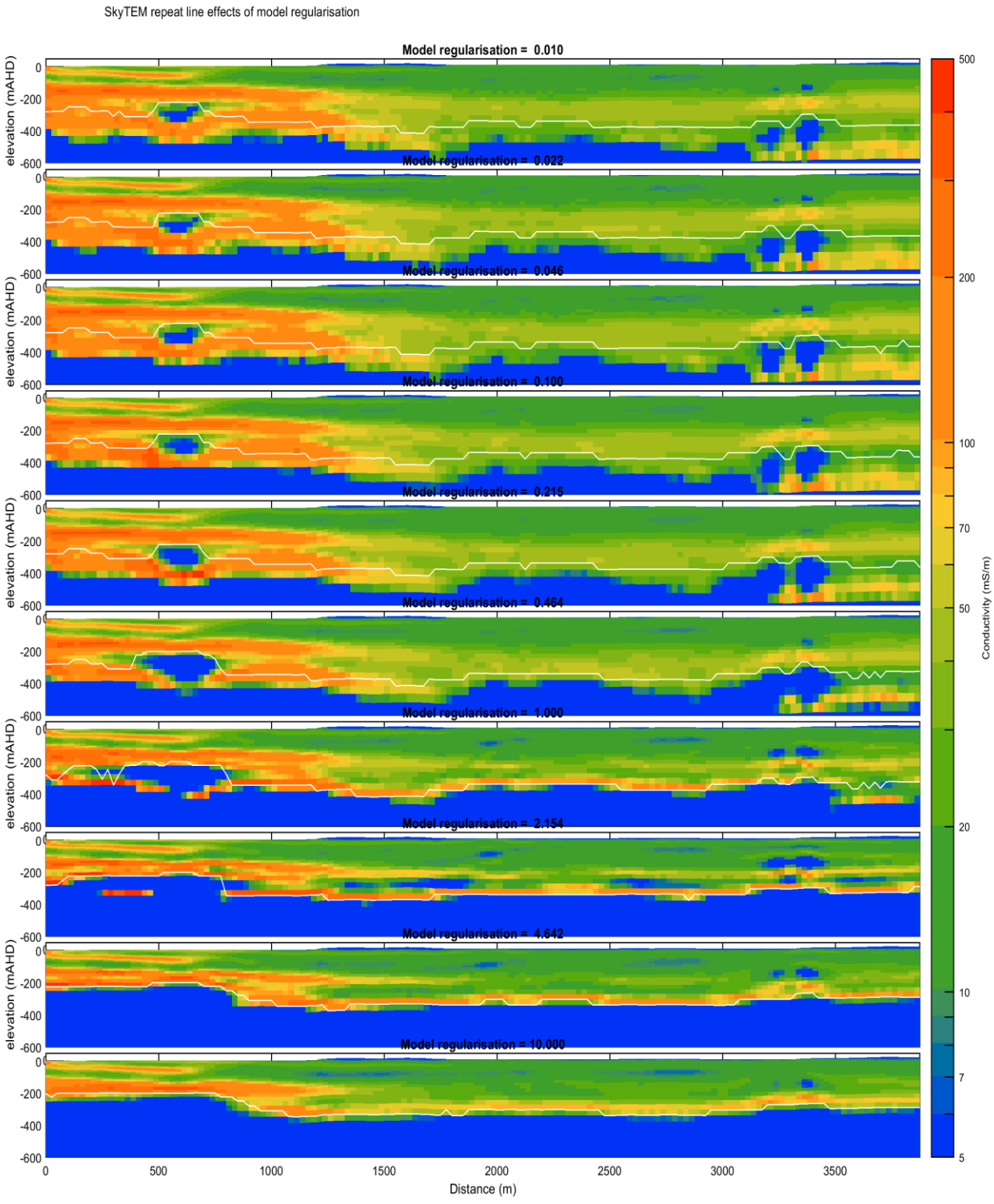

Figure 4-4: Inversions showing the effect of model regularisation for a wide range of regularisation weighting values (α). All inversion runs were initialised with the same starting model. The model regularisation structure for each is the same. A depth of investigation (DOI) line is shown in white. There is very little variation in models above the DOI when regularisation parameter α is below 1.

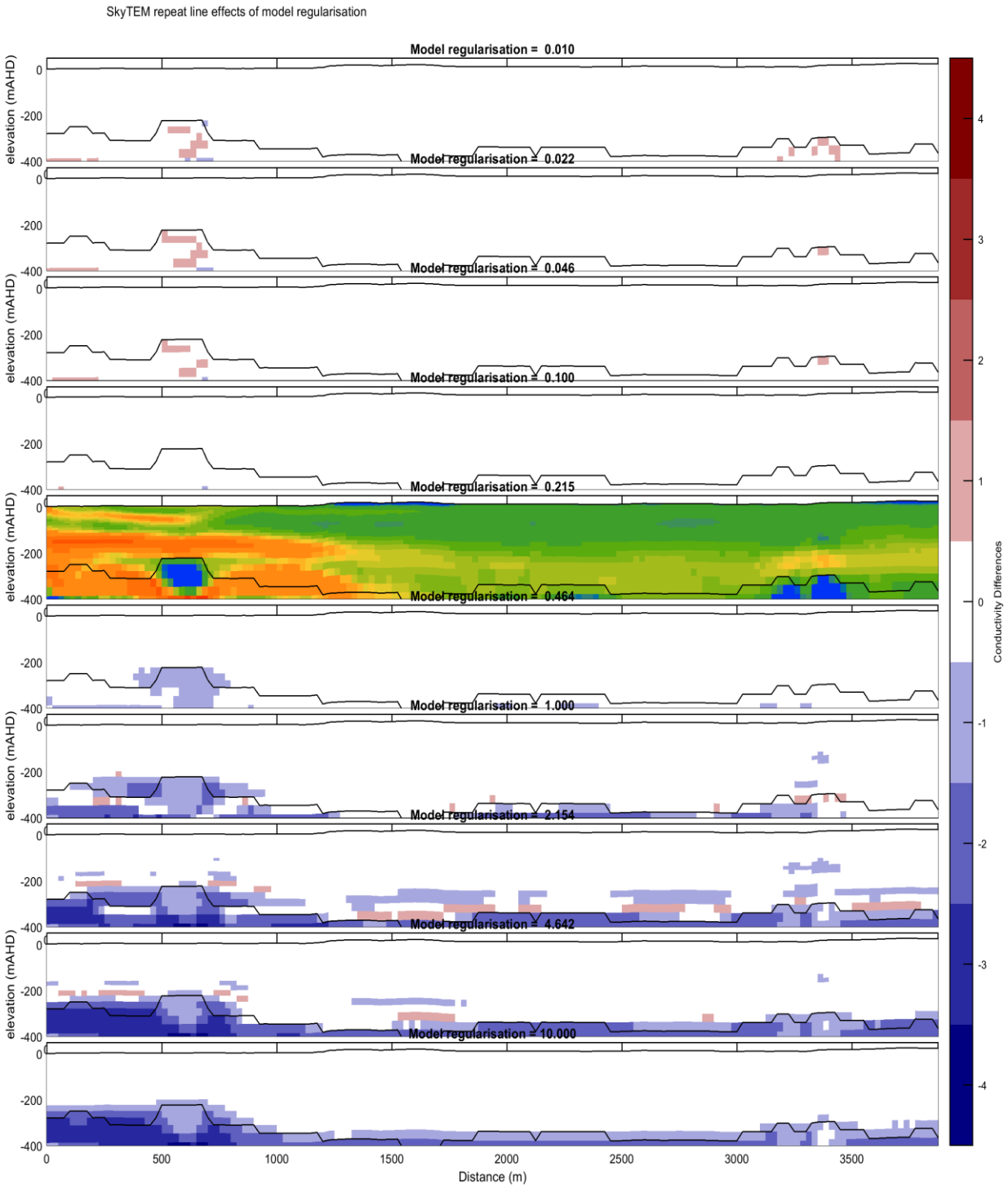

Figure 4-5: Plots of the differences in the inversion models from the comparison model at regularisation value 0.215. differences are in the log base 10 of conductivity. We can see that each model agrees with the comparison model, within a factor of 10, above the depth of investigation line.

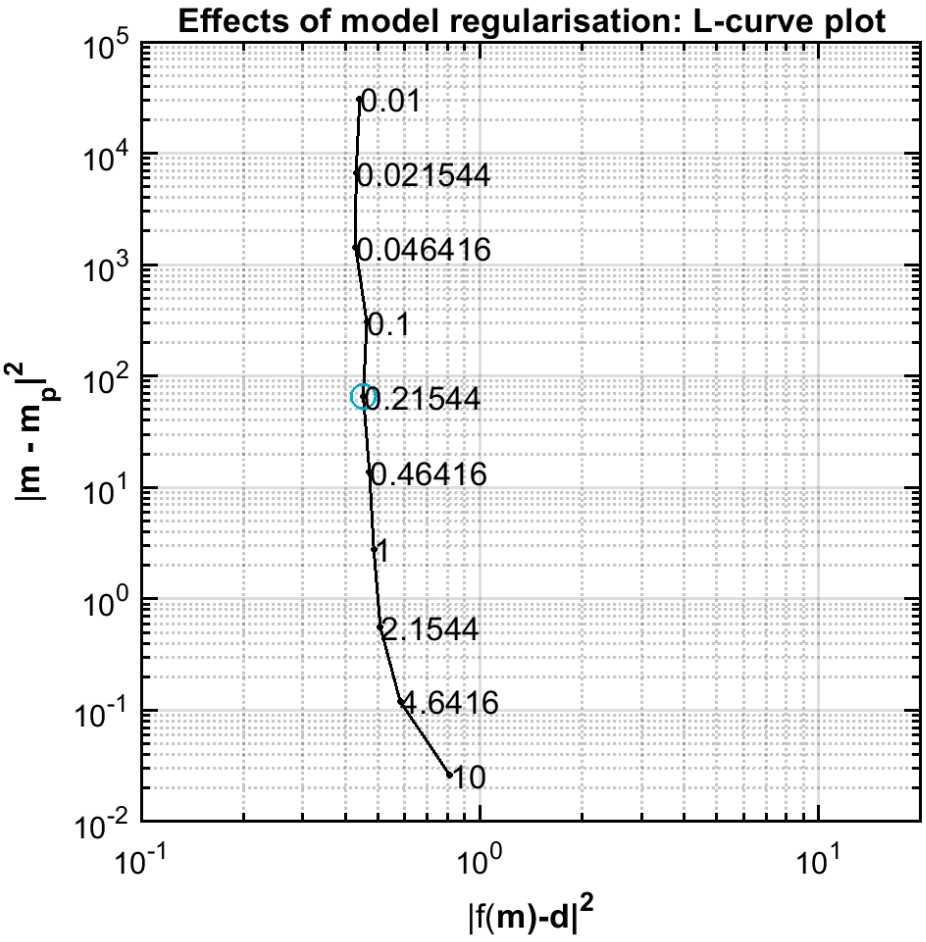

Figure 4-6: Plot of data misfit versus model misfit (L-Curve) for the inversion products shown in Error! Reference source not found.**. with varying (α). The parameter of 0.215, which is near the maximum curvature of the L-Curve is chosen for all inversions.**

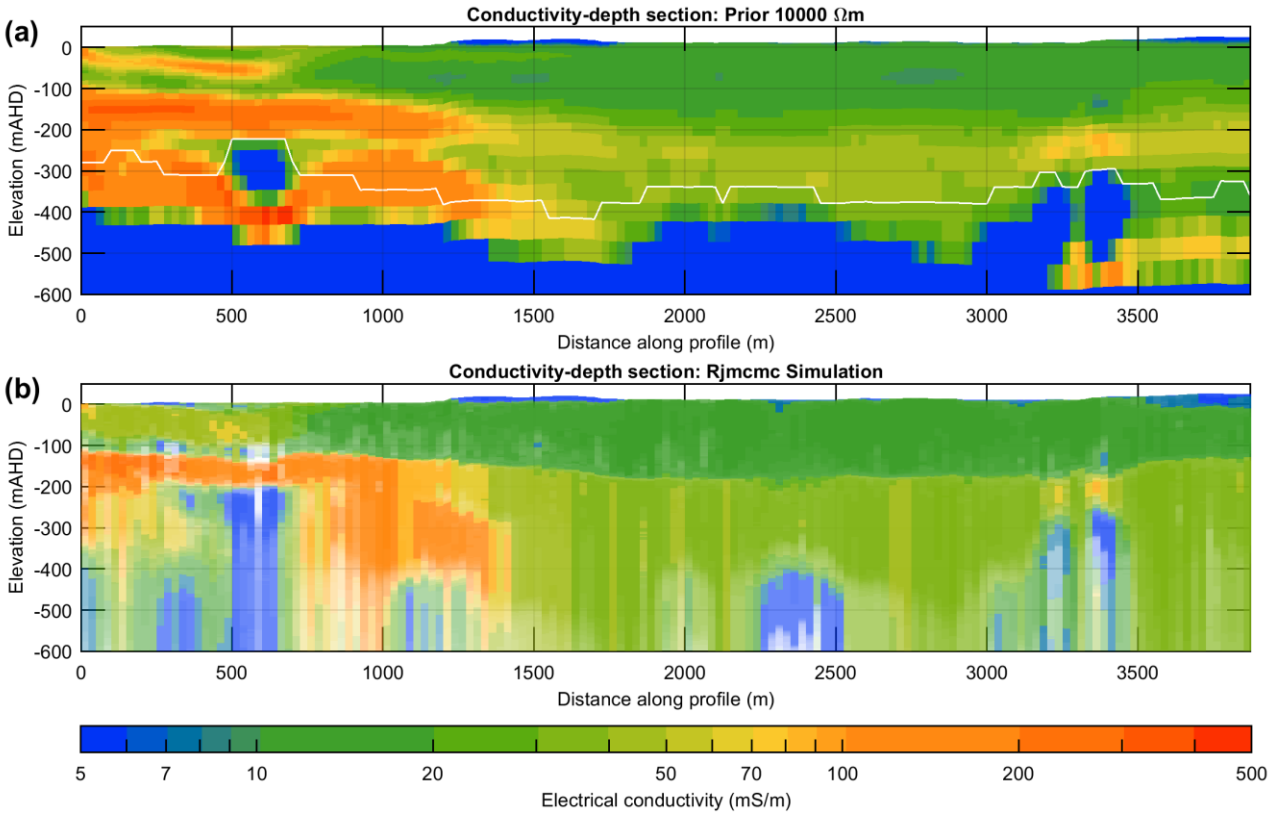

Figure 4-7: Comparison of (a) deterministic inversion with a regularisation parameter of 0.215 to (b) the RJMCMC simulation models for repeat line 1.

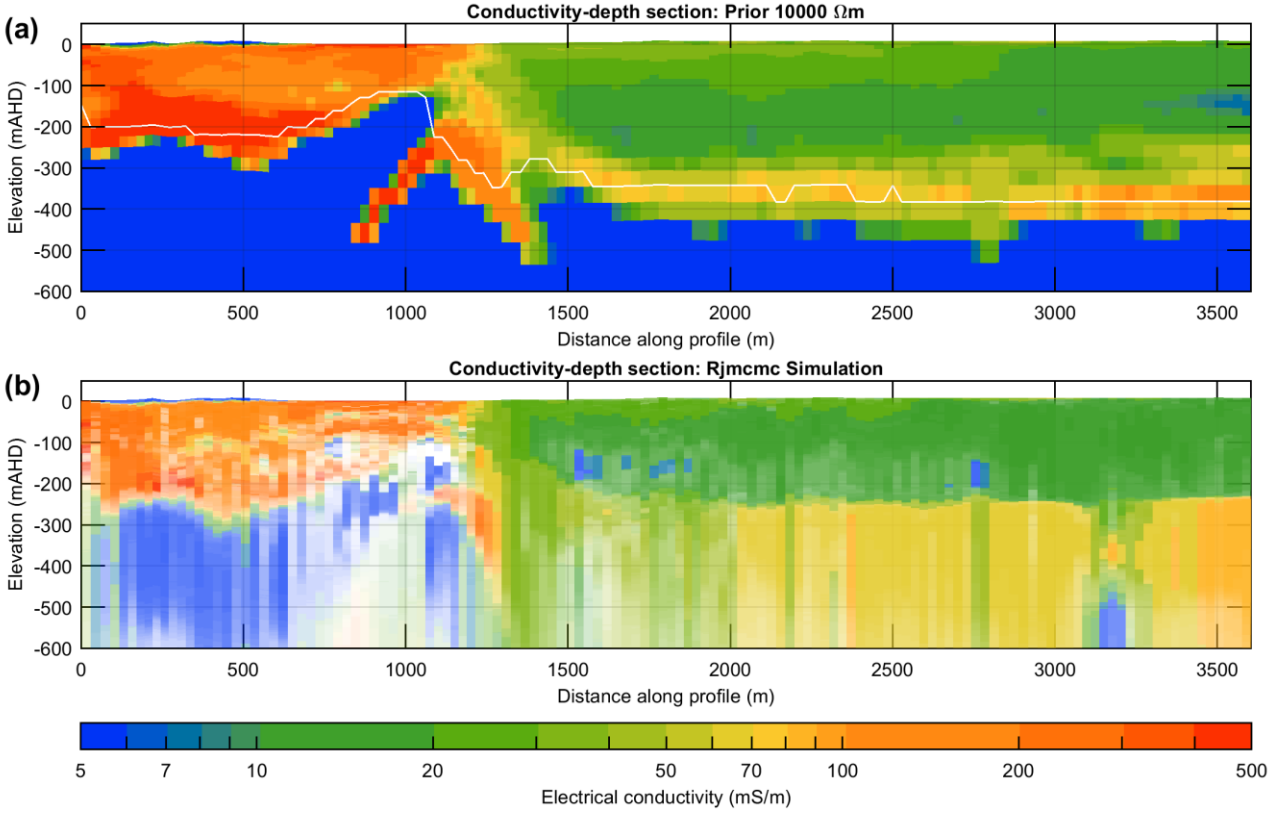

Figure 4-8: Comparison of (a) deterministic inversion with a regularisation parameter of 0.215 to (b) the RJMCMC simulation models for repeat line 2.

4.5 Effect of Prior on Inversion

Finally, we examine the effect that the prior resistivity model has on the inverted data. The objective function in Equation (4) shows that the model misfit calculation in the second term of the right-hand side encourages the inversion to honour the prior resistivity vector $\boldsymbol{m_p}$. The degree to which the inverted model must reflect the prior resistivity is governed by the model regularisation matrix $\boldsymbol{C_m^{-1}}$ and the regularisation parameter α. Figure 4-9a shows the inversion results when $\boldsymbol{m_p}$ is set to a homogeneous half space with resistivity equal to 10000 Ωm (0.1 mS/m), and Figure 4-9b shows the inversion model when the prior resistivity is set to a relatively conductive half space of 1 Ωm (1000 mS/m).

Comparison of Figure 4-9a and b show that there is remarkable similarity in the inverted models in the near surface where the data is very informative to the model structure. The differences between the inversion models begin to appear noticeable below the depth of investigation lines in the figures. However, examination of the total misfit for the inversions, shown in Figure 4-9d, reveals very little difference. The obvious implication of these results is that it is only where the inverted models are similar that they have any effect on the measured data. We can immediately extend this analysis by computing a mean model of the two inversion models. Figure 4-9c displays a conductivity depth section that is created from the geometric mean of the models in a and b using the equation

$$\bar{\boldsymbol{m}} = \sqrt{\boldsymbol{m_{10000}} \cdot \boldsymbol{m_1}} = \exp((\log(\boldsymbol{m_{10000}}) + \log(\boldsymbol{m_1}))\,/\boldsymbol{2}) \quad \textbf{(5)}$$

where $\boldsymbol{m_{10000}}$ is the model resulting from the inversion with the 10000 Ωm prior resistivity, $\boldsymbol{m_1}$ is the model from the inversion with the 1 Ωm prior resistivity, and $\bar{\boldsymbol{m}}$ is the mean model. We can calculate the total misfit for model $\bar{\boldsymbol{m}}$ by adjusting Equation (4) so that the new prior resistivity has a value of 100 Ωm. The misfit for this model, and the $\boldsymbol{m_{10000}}$ and $\boldsymbol{m_1}$ models are shown in Figure 4-9d.

In addition to calculating the geometric mean of the two inversions, we can also calculate the difference factor to measure the similarity of the $\boldsymbol{m_{10000}}$ and the $\boldsymbol{m_1}$models. By keeping the inversion products in logarithmic space, the differences between the $\boldsymbol{m_{10000}}$ and the $\boldsymbol{m_1}$ are equivalent to ratios between resistivity in the linear space. We see, then, that if the resistivity at a given location from the $\boldsymbol{m_{10000}}$ model is 200 Ωm, and the resistivity at that location in the $\boldsymbol{m_1}$ model is 50 Ωm, then the resistivity in the $\bar{\boldsymbol{m}}$ model is 100 Ωm. The difference ratio between the $\boldsymbol{m_{10000}}$ and the $\boldsymbol{m_1}$ models is 2. If the difference ratio at that location was 4, then the $\boldsymbol{m_{10000}}$ value at that location could be 400 Ωm and the $\boldsymbol{m_1}$ could be 25 Ωm. We now add transparency to the geometric mean inversion model based on the resistivity ratios from the $\boldsymbol{m_{10000}}$ and $\boldsymbol{m_1}$ models.

Areas where the resistivity ratio is less than 2 have no transparency. Because the transparency scale indicates regions where the resistivity ratios are less than 2, and they are not continuous from the surface, we have decided to rename the transparency shading as 'regions of investigation' rather than 'depth of investigation', since they indicate volumes in the model that are insensitive to the prior model and, hence, can be regarded as being relatively well-determined by the data. We repeat the analysis for repeat line 2 in Figure 4-10.

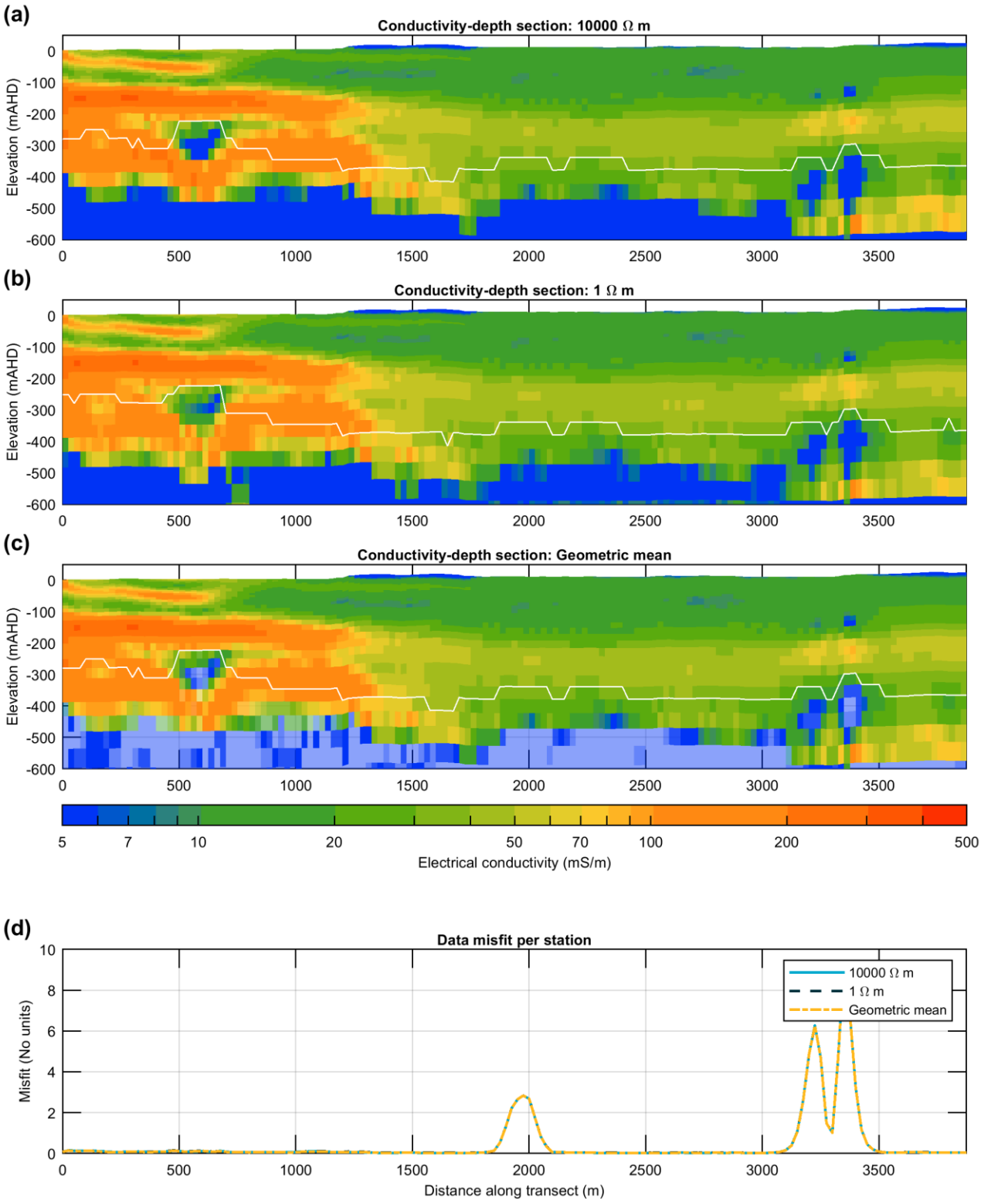

Figure 4-9: Comparisons of inversion results for repeat line 1 with different prior conductivities. (a) Inversion with a 10000 Ωm half-space prior model. (b) Inversion with a 1 Ωm prior model. (c) Compiled model taken from the geometric mean of the 10000 Ωm and 1 Ωm models. (d) Data misfit for each of the 3 models in (a) – (c).

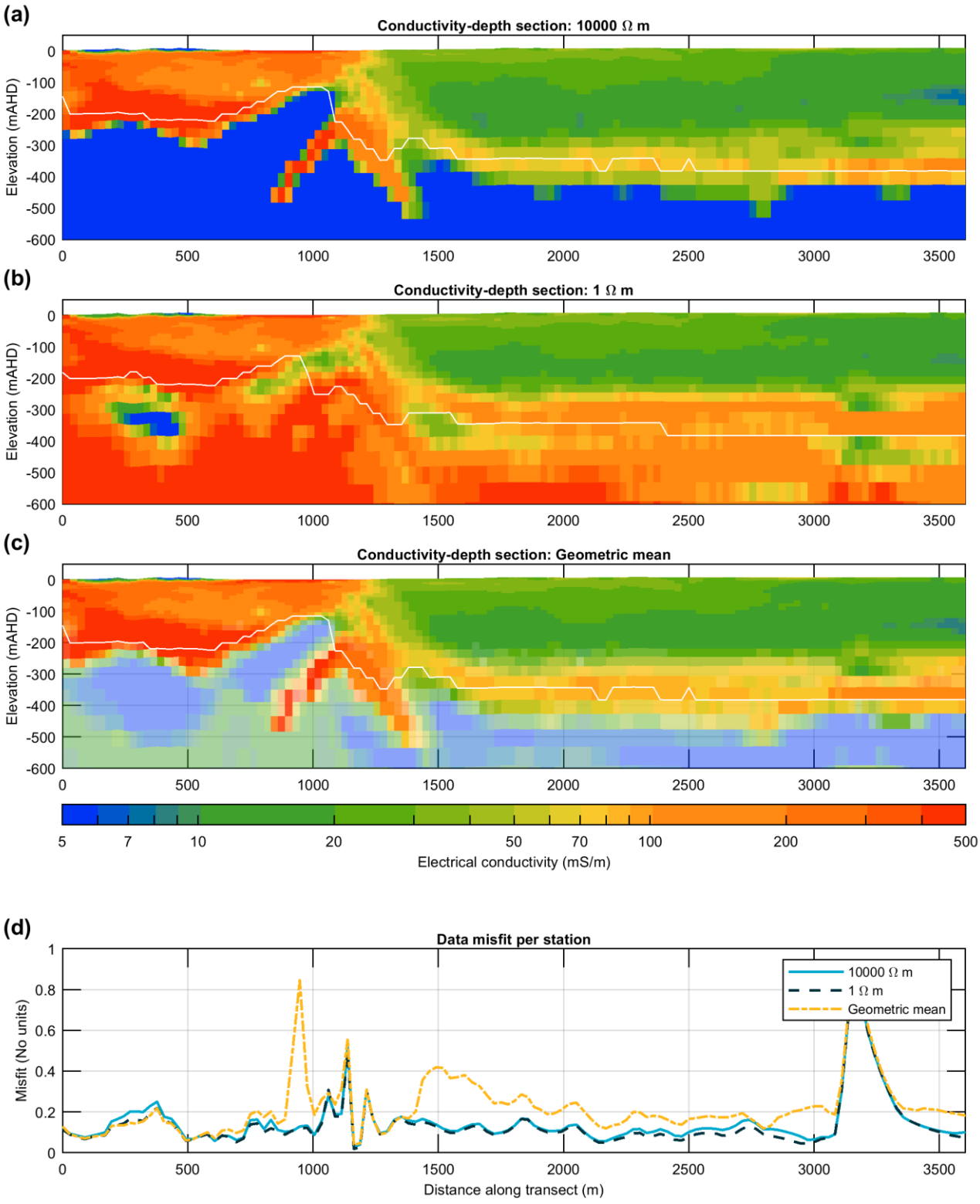

Figure 4-10: Comparisons of inversion results for repeat line 2 with different prior conductivities. (a) Inversion with a 10000 Ωm half-space prior model. (b) Inversion with a 1 Ωm prior model. (c) Compiled model taken from the geometric mean of the 10000 Ωm and 1 Ωm models. (d) Data misfit for each of the 3 models in (a) – (c).

4.6 Combining regularisation and prior models

We are now in the position to show how the selection of an appropriate regularisation term and the use of prior conductivity values in the inversion. The regularisation parameter adjusts the smoothness of the inversion model, and the prior conductivity values in the inversion algorithm indicate which model parameters are important for the data misfit term in the objective function (Equation (4)). We will do this by reproducing Figure 4-7 and Figure 4-8 but using the geometric model and the model shading resulting from the inversions with differing prior conductivities. The results are shown in Figure 4-11 and Figure 4-12. We can see excellent agreement between the RJMCMC models and the deterministic inversions.

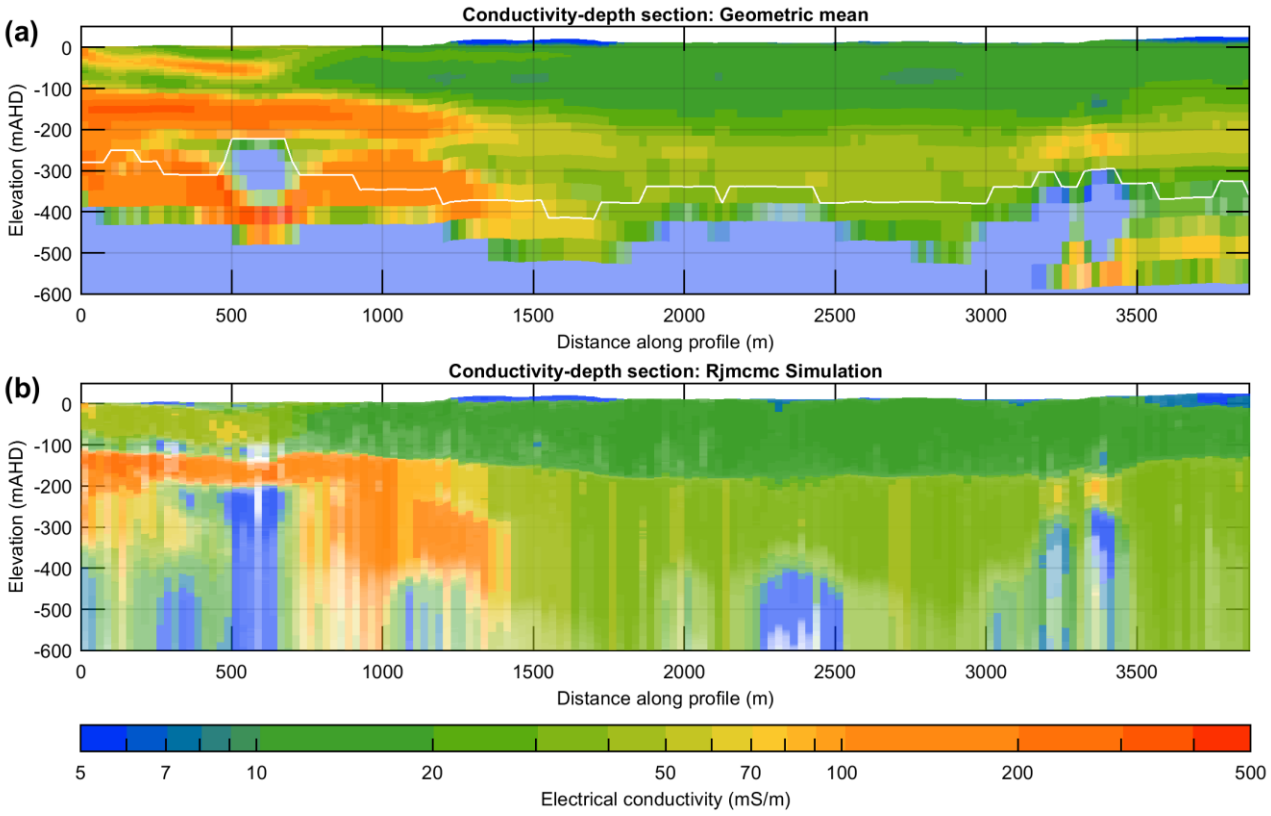

Figure 4-11: Comparison of (a) the combined deterministic inversion with a regularisation parameter of 0.215 and parameter shading based on 2 different prior models to (b) the RJMCMC simulation models for repeat line 1.

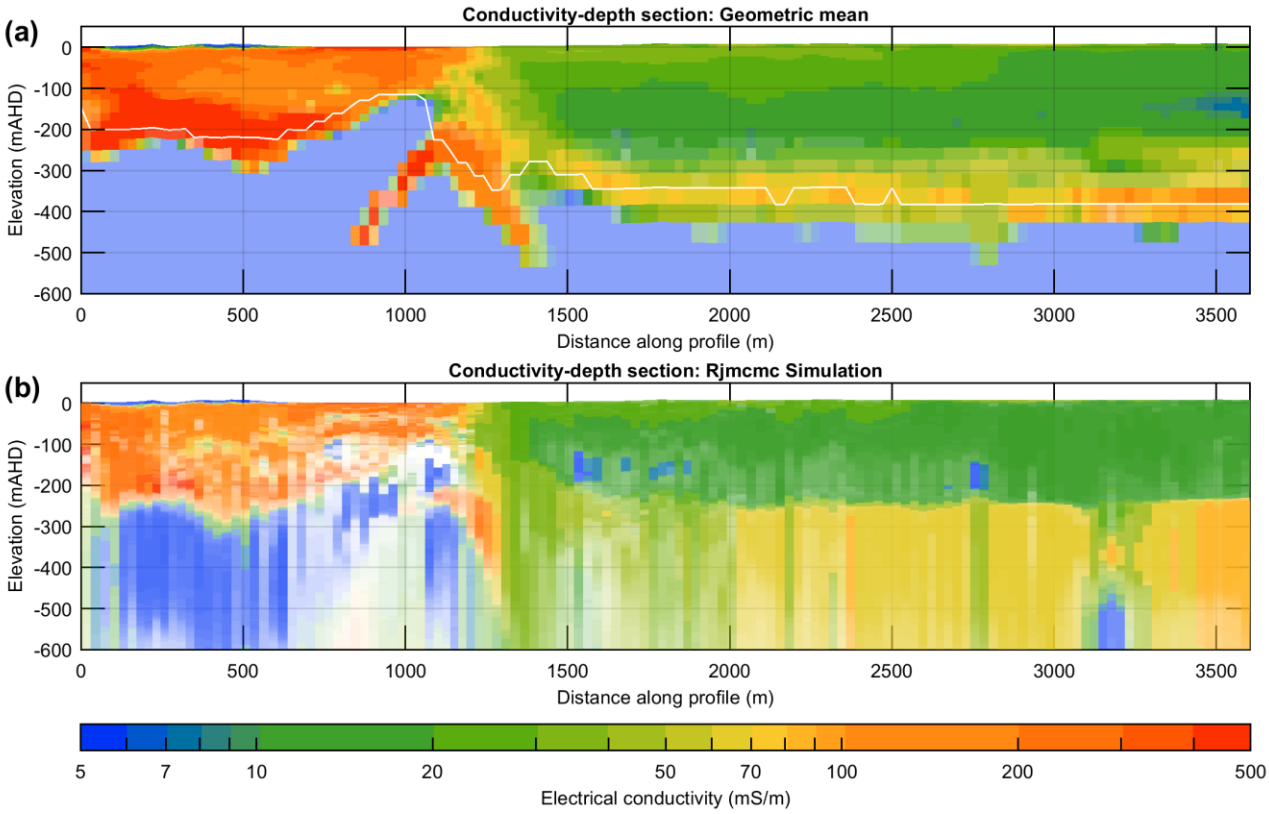

Figure 4-12: Comparison of (a) the combined deterministic inversion with a regularisation parameter of 0.215 and parameter shading based on 2 different prior models to (b) the RJMCMC simulation models for repeat line 2.

5 Results

5.1 Spatially Constrained Inversion – Model Results

The Limestone Coast SkyTEM survey data were inverted using a smooth layer 1D layered Earth inversion. This type of model typically consists of 15-30 layers with fixed thicknesses, often increasing with depth. The amount the conductivity of one layer can vary to the next is defined by a vertical constraint (e.g. a predefined thickness). The considerable number of layers and the gradual change in conductivity in this type of model makes the resulting models appear continuous. This in turn can make it difficult to pick layer boundaries as these may appear diffuse. However, this may be more representative of the interface between the SWI and fresh water in the coastal aquifers.

For the purposes of this study, a 30-layer model was used. The first layer thickness was selected to be 1m with logarithmically increasing thickness to a depth of 670m, which is the depth of the last layer boundary. Modelling employed a Spatially Constrained Inversion (SCI) methodology described by (Viezzoli et al. 2008). The SCI, a quasi-3D inversion methodology, is based on a 1D forward response, with 3D spatial constraints. The spatial constraints allow prior information (e.g. expected (hydro) geological variability) to migrate along/through the entire dataset (Figure 5-1). This type of inversion uses constraints along lines and across lines, which means that layer parameters are connected between adjacent soundings.

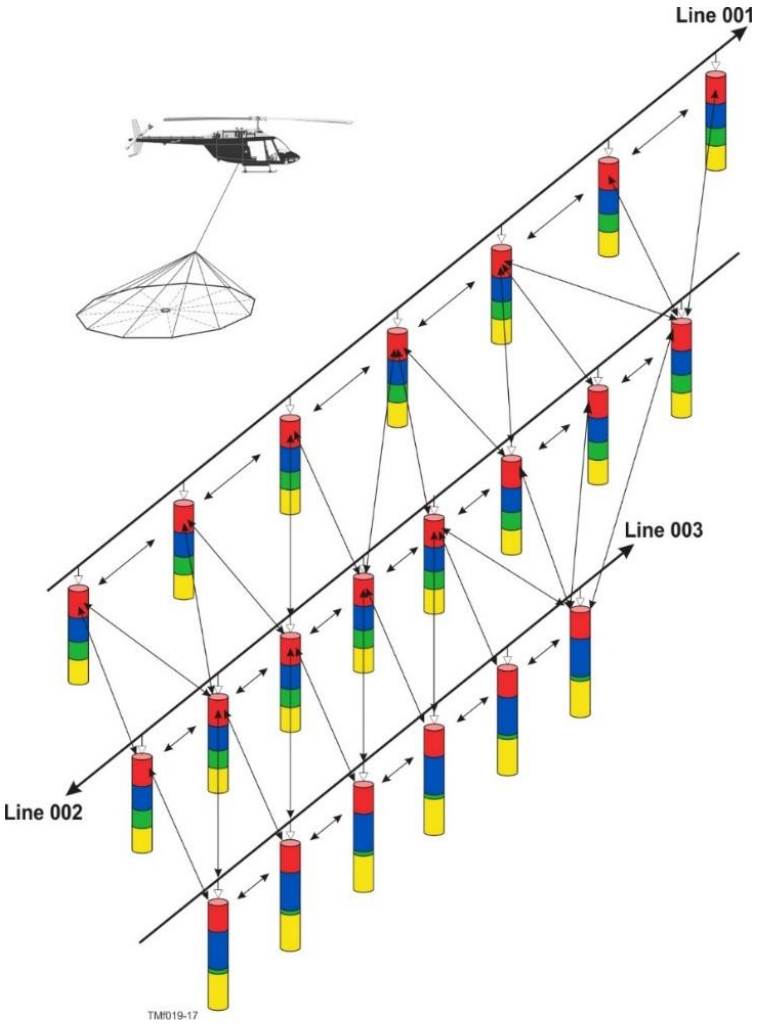

Figure 5-1: Schematic describing the process of allowing prior information to migrate along or through a series of soundings acquired by an AEM system when they are inverted using the Spatially Constrained Inversion procedure (SCI). In the case of the Limestone Coast, prior information is allowed to proceed from sounding to sounding along and across the flight lines.

The inversion solved both the Low and High Moment Z-component data. This approach yields the maximum possible resolution of model parameters, as the Low Moment contains information from the near surface,

and the High Moment information relating to the deeper part of the models. As mentioned in, Section 3-2 subsurface conductivity can be presented in section and plan form. Conductivity-depth sections generated for the Limestone coast AEM survey have been produced for each of the flown lines. They are reproduced in the accompanying project report (Davis and Munday 2025). Conductivity-depth intervals have been generated for a series of depths, increasing logarithmically with depth.

5.2 Conductivity-depth sections

An example of an electrical conductivity depth section is shown in Figure 5-2. Results from the modelling of each line are presented in an accompanying Report (Davis and Munday 2025). The top panel shows the flight path of the survey line in plan view, the next panel shows the normalised data misfit of each station along the survey line, the data misfit section shows the difference between predicted and measured data, weighted by the data noise, for each station, and the bottom panel shows the modelled electrical conductivity along the flight line. Note the electrical conductivity is scaled to logarithm base 10.

5.3 Conductivity-depth intervals

A suite of conductivity-depth intervals, representing the average conductivity for a specified depth interval beneath the surface have been generated from the smooth model inversion described in section 4. A representative set is presented in Figures 5-3 to 5-9.

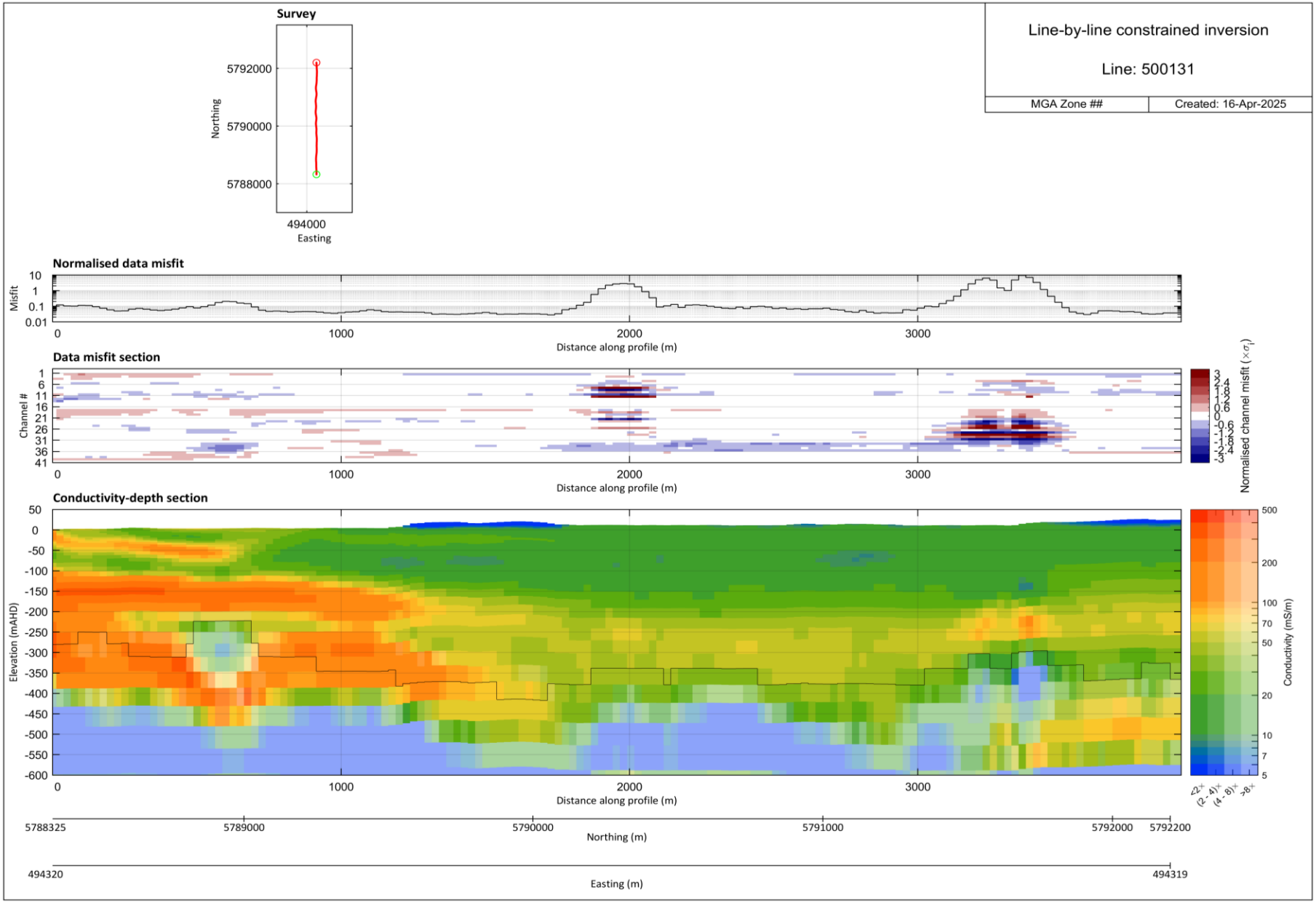

Figure 5-2 An example of an electrical conductivity section resulting from inversion of the electromagnetic survey data.

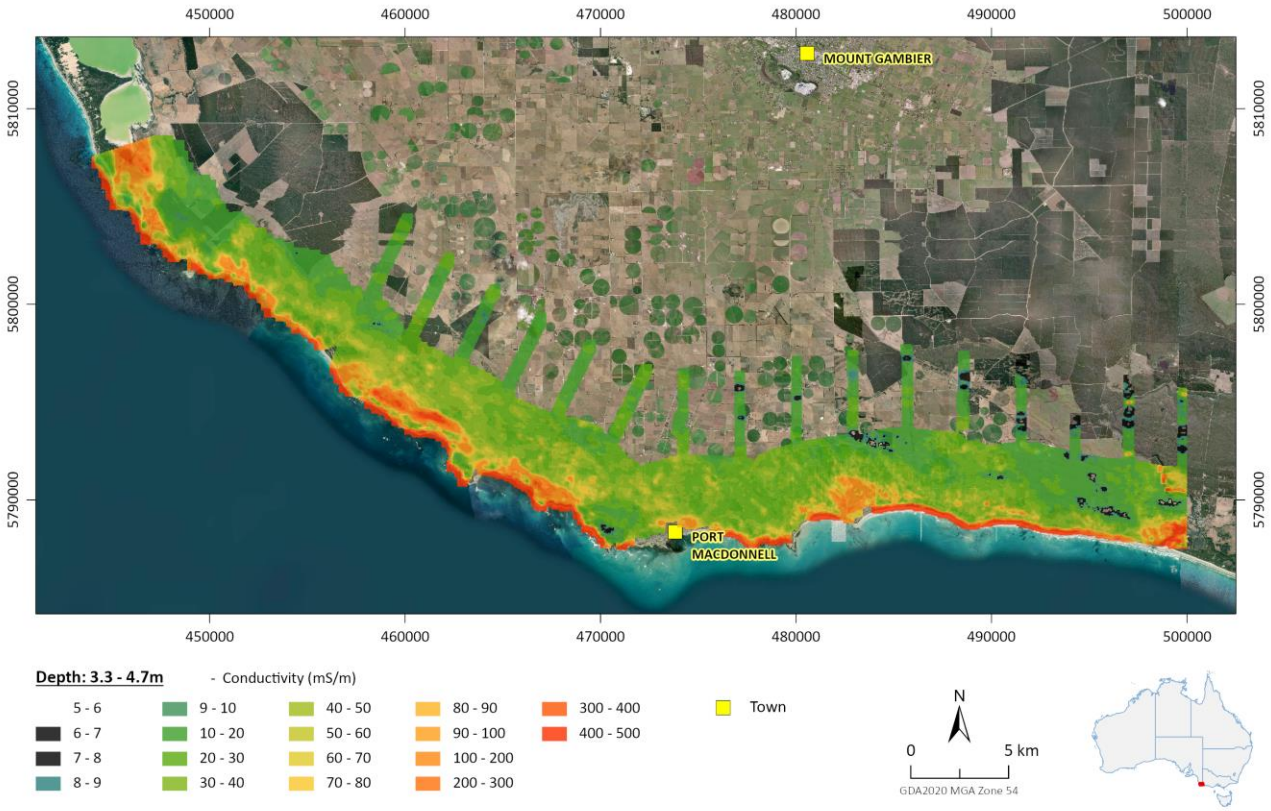

Figure 5-3: Conductivity-depth interval for 3.3-4.7m below the ground surface,

Figure 5-4: Conductivity-depth interval for 19.7-22.9m below the ground surface

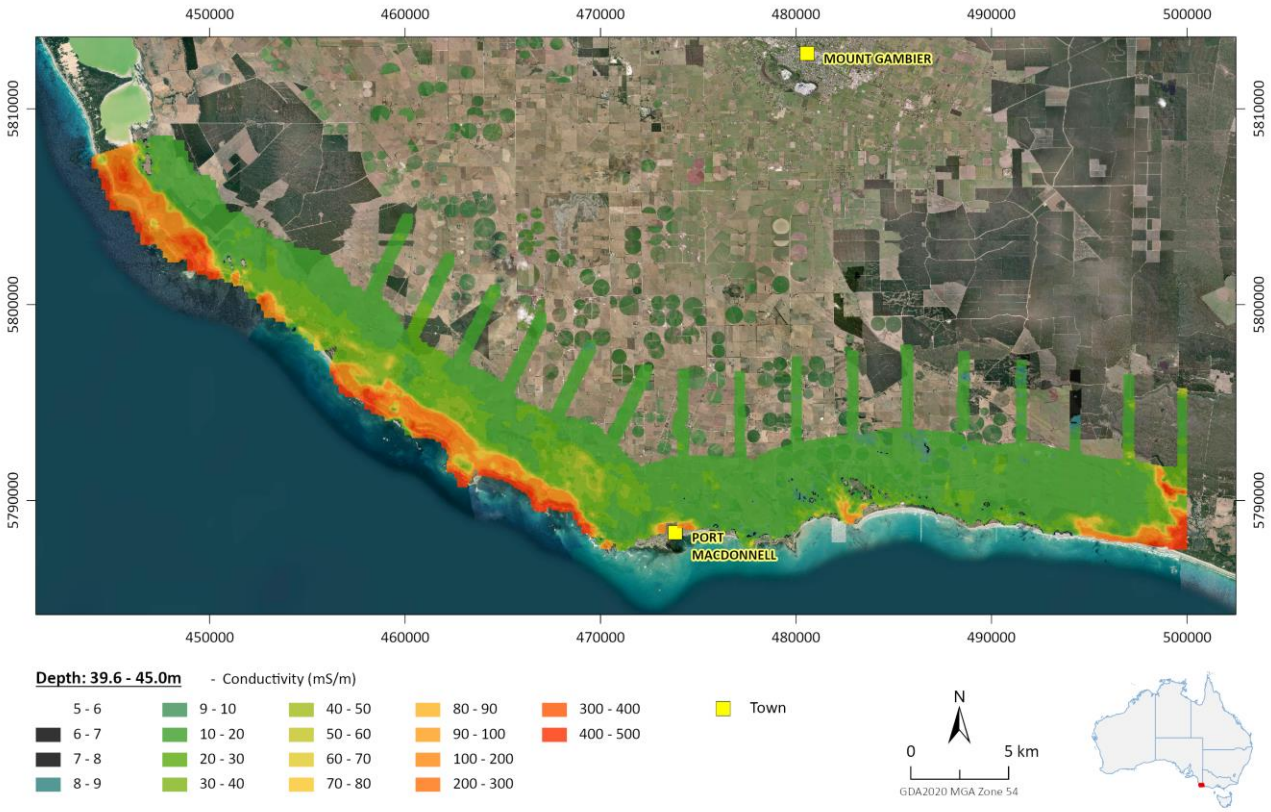

Figure 5-5: Conductivity-depth interval for 39.6-45m below the ground surface,

Figure 5-6 Conductivity-depth interval for 92.6 – 103.8m below the ground surface.

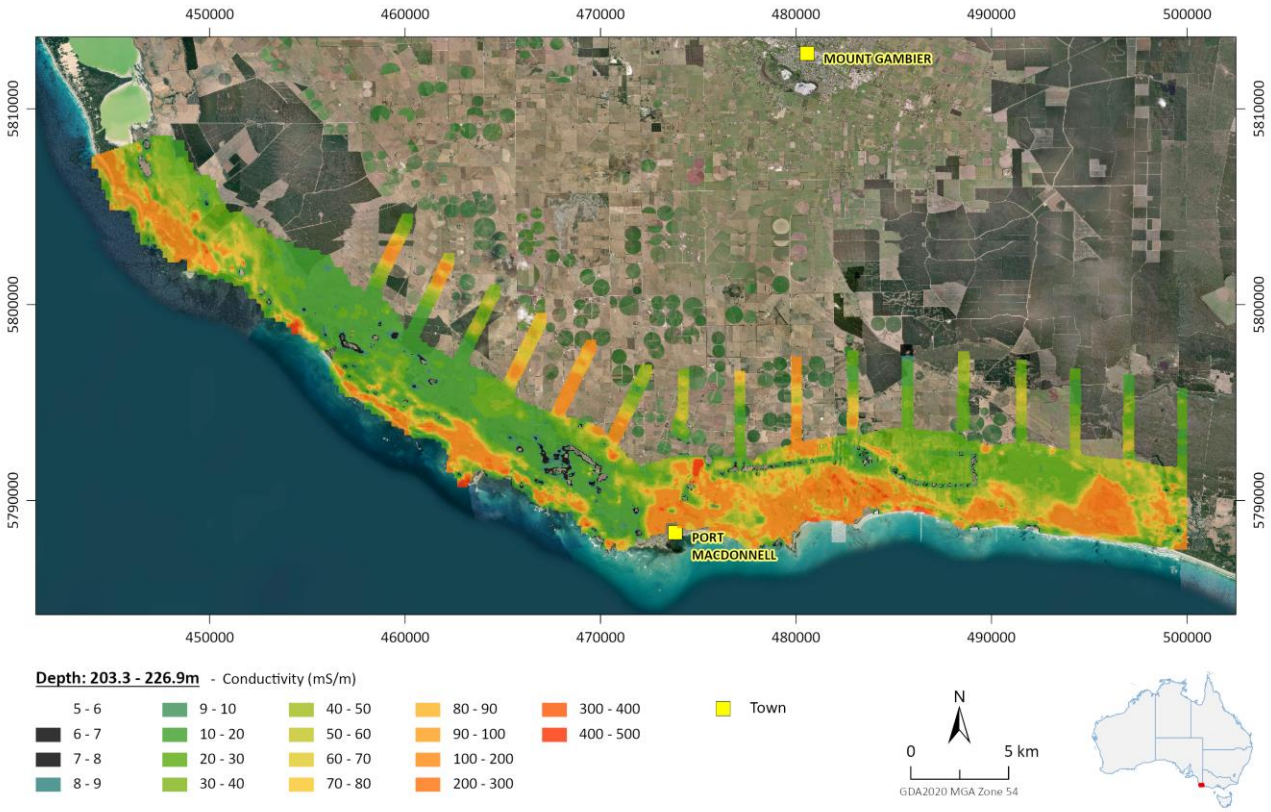

Figure 5-7: Conductivity-depth interval for 203.3-226.9m below the ground surface.

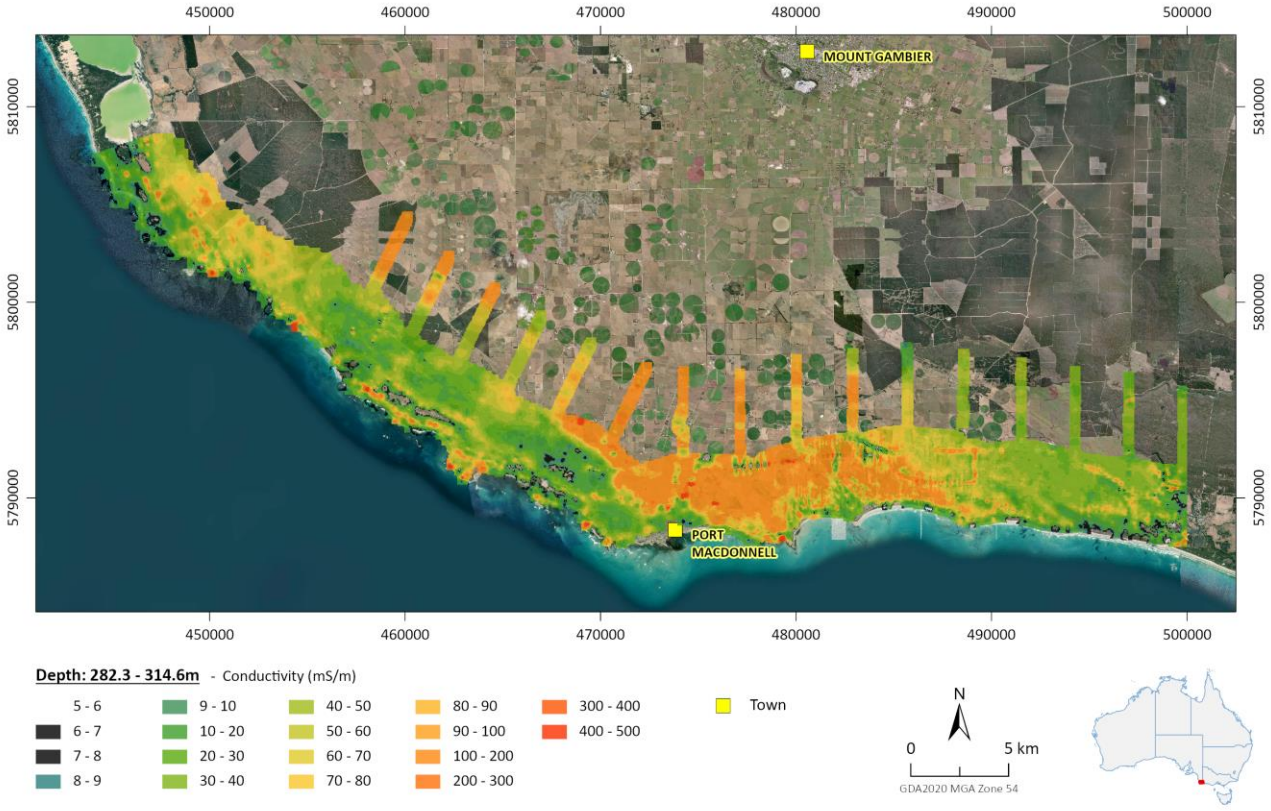

Figure 5-8: Conductivity-depth interval for 282-314.6m below the ground surface.

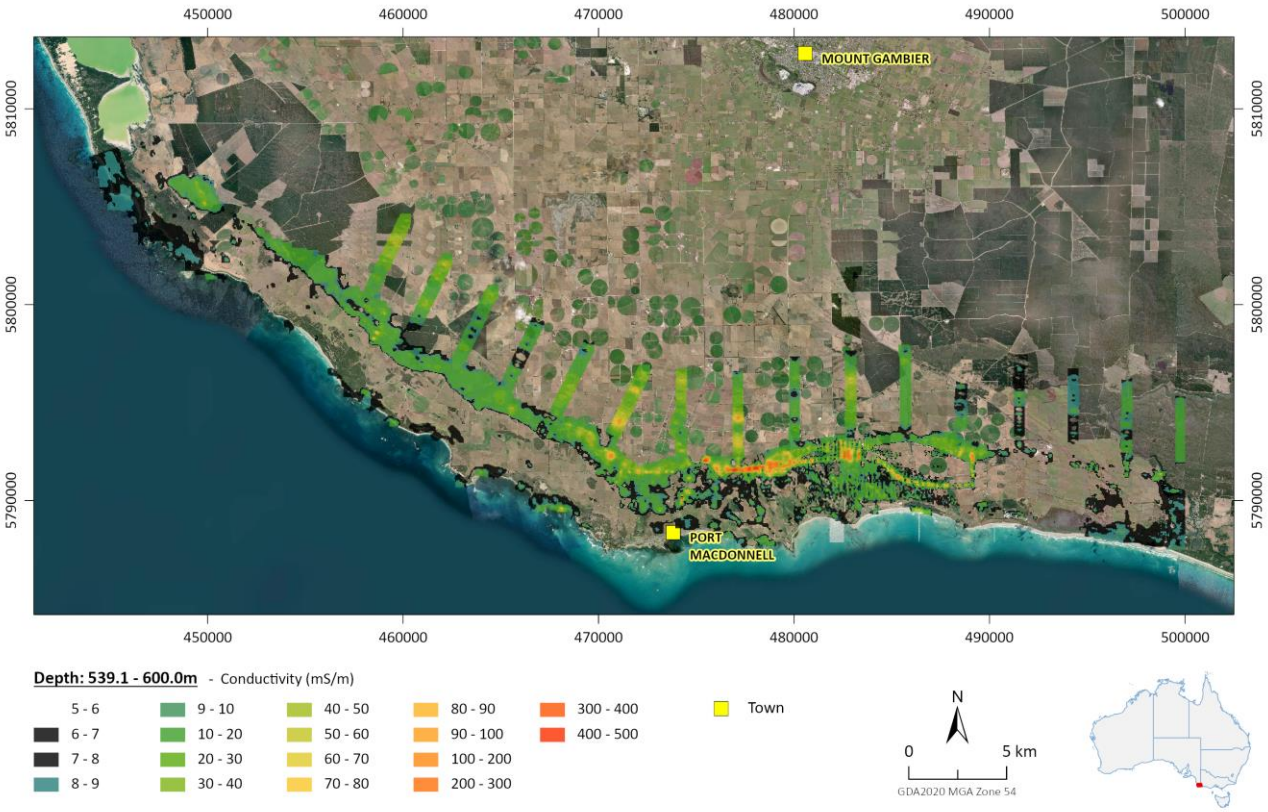

Figure 5-9: Conductivity-depth interval for 539-600m below the ground surface

6 Summary

Inversion of airborne electromagnetic data covering the SE coastal region has resulted in the generation of a spatially consistent 3D model of the subsurface electrical conductivity structure of the region. This spatial continuity provided by this model permits an improved understanding of the interaction between coastal aquifers and the sea, particularly as the extent and geometry of the saltwater interface can be resolved.

The modelled conductivity structure suggests a complex interaction between the regional groundwater system, lithology and the ocean. This is exemplified by the irregularity of the saltwater interface along this stretch of the coast, and in particular the unevenness of its ingress inland. Figures 5-3 to 5-5 illustrate this complexity, with the conductivity structure indicating that the SWI may extend more than a kilometre inland in places, but that this is not spatially consistent along the stretch flown in this survey. Further studies are warranted to fully explore the relationship between modelled conductivity structure, the coastal aquifers, their properties and the saltwater interface.

7 References

Annetts D, Ibrahimi T, Davis A, George R, Cahill K, Munday T and Paul R (2015) 'The application of AEM to mapping sea-water intrusion at La Grange, WA', *ASEG Extended Abstracts*, 2015(1):1–4, doi:10.1071/ASEG2015ab164.

Auken E, Christiansen AV, Jacobsen BH, Foged N and Sørensen KI (2005) 'Piecewise 1D laterally constrained inversion of resistivity data', *Geophysical Prospecting*, 53(4):497–506, doi:10.1111/j.1365-2478.2005.00486.x.

Brandes de Roos I, Jenke G and Brown D (2010) The use of SkyTEM geophysics in a salt water intrusion setting Extended Abstract, SWIM21 - 21st Salt Water Intrusion MeetingJune 21 - 26, 2010 Azores, Portugal

Christiansen AV and Auken E (2012) A global measure for depth of investigation, *Geophysics*, 77(4):WB171–WB177.

Davis A and Munday TJ (2025) Limestone Coast Airborne Electromagnetic Survey: Conductivity-Depth Sections. Goyder Institute for Water Research Technical Report Series No. 25/5.2.

Davis, AC, Munday, TJ and George, RJ (2015) Gascoyne River airborne electromagnetic survey II: Inversion Report. CSIRO: Water for a Healthy Country Flagship Technical Report; CSIRO Technical Report EP-13-11-758. 158pp.

Emerson D and Yang Y (1997) 'Effects of water salinity and saturation on the electrical resistivity of clays', *Preview*, 68:19–24.

Foged N, Auken E, Christiansen AV and Sørensen KI (2013) 'Test-site calibration and validation of airborne and ground-based TEM systems', *Geophysics*, 78(2):E95–E106, doi:10.1190/geo2012-0244.1.

Geofysiksamarbejdet (2012) Refinement of the national TEM reference model at Lyngby. http://www.hgg.geo.au.dk/rapporter/Refinement_TEM_Ref_Model_Lyngby_Update_June_2012.pdf

Gilgallon K and McGivern M (2018) The use of Airborne EM to investigate coastal carbonate aquifer, seawater intrusions and sustainable borefield yield at Exmouth, Western Australia, ASEG Extended Abstracts, 2018:1, 1-6, DOI:

Goebel M, Knight R and Halkjær M (2019) 'Mapping saltwater intrusion with an airborne electromagnetic method in the offshore coastal environment, Monterey Bay, California', *Journal of Hydrology: Regional Studies*, 23:100602, doi:10.1016/j.ejrh.2019.100602.

Green A and Lane R (2003) 'Estimating Noise Levels in AEM Data', *ASEG Extended Abstracts*, 2003(2):1, doi:10.1071/ASEG2003ab093.

Green PJ (1995) Reversible jump Markov chain Monte Carlo computation and Bayesian model determination, *Biometrika*, 82(4):711–732, doi:10.1093/biomet/82.4.711.

Hansen PC (1998) *Rank-Deficient and Discrete Ill-Posed Problems: Numerical Aspects of Linear Inversion*, Society for Industrial and Applied Mathematics, doi:10.1137/1.9780898719697.

Jorgensen F and Sandersen P (2013) Results from a 10-year AEM Mapping Programme of Buried Tunnel Valleys in Denmark, *Second International Conference on Engineering Geophysics*, Al Ain, United Arab Emirates, doi:10.3997/2214-4609.20131868.

Kirkegaard C, Sonnenborg TO, Auken E and Jørgensen F (2011) 'Salinity Distribution in Heterogeneous Coastal Aquifers Mapped by Airborne Electromagnetics', *Vadose Zone Journal*, 10(1):125–135.

Lane, R (2000) Conductive unit parameters: summarising complex conductivity distributions. 70th Meeting, SEG, Calgary, Expanded Abstracts, Volume 1, Section EM 4.2, p. 328-331.

Lane R (2002) Ground and Airborne Electromagnetic methods. In Geophysical and Remote Sensing Methods for Regolith Exploration. (Ed É Papp) pp. 53-79. CRC LEME Open File Report 144. CRC LEME, Perth.

Lane R and Pracilio G (2000) 'Visualisation of Sub-Surface Conductivity Derived from Airborne EM', in *Symposium on the Application of Geophysics to Engineering and Environmental Problems 2000*, , Environment and Engineering Geophysical Society, doi:10.4133/1.2922705.

Lawrie, KC, Christensen, JB, Clarke, J, Ivkovic, KM and Marshall, SK (2012) Evaluating the role of airborne electromagnetics in mapping seawater intrusion and carbonate-karstic graoundwater systems in Australia: Geoscience Australia Record 2012/42

Levenberg K (1944) A method for the solution of certain non-linear problems in least squares, *Quarterly of Applied Mathematics*, 2(2):164–168, doi:10.1090/qam/10666.

Macnae J (2011) Airborne EM system comparison, in *Proceedings of the 10th SEGJ International Symposium, Kyoto, Japan, 20-22 November 2011*, *Proceedings of the 10th SEGJ International Symposium*, Society of Exploration Geophysicists of Japan, Kyoto, Japan, doi:10.1190/segj102011-001.48.

Macnae, J (2007) Broadband airborne electromagnetics, Proceedings of Exploration 2007, Toronto, Canada.

Marquardt DW (1963) An Algorithm for Least-Squares Estimation of Nonlinear Parameters, *Journal of the Society for Industrial and Applied Mathematics*, 11(2):431–441, doi:10.1137/0111030.

McNeil JD (1980) *Electromagnetic terrain conductivity measurement at low induction numbers*, Geonics Ltd, Ontario.

McNeil, JD (1990) Use of electromagnetic methods for groundwater studies: Investigations in Geophysics No.5, Geotechnical and Environmental Geophysics, S.H. Ward (ed), SEG, 191–218.

Minsley BJ, Foks NL and Bedrosian PA (2021) Quantifying model structural uncertainty using airborne electromagnetic data, *Geophysical Journal International*, 224(1):590–607, doi:10.1093/gji/ggaa393.

Munday, TJ, Soerensen, CC, Mule, S, Cahill, K, Taylor, AR, Houthuysen, L, Ellis, J and Ibrahimi, T (2020) Hydrogeophysical Investigation of South Goulburn Island, Northern Territory. CSIRO Technical Report EP206973; CSIRO, Australia.

Mustafa S, Slater S and Barnett S (2012) Preliminary investigation of seawater intrusion into a freshwater coastal aquifer – Lower South East, DEWNR Technical Report 2012/01, Government of South Australia, Department of Environment, Water and Natural Resources, Adelaide

Newman GA, Anderson WL and Hohmann GW (1987) Interpretation of transient electromagnetic soundings over three-dimensional structures for the central-loop configuration, *Geophysical Journal International*, 89(3):889–914, doi:10.1111/j.1365-246X.1987.tb05200.x.

Palacky, GJ (1983) Tutorial: Research, applications and publications in electrical and electromagnetic methods: Geophysical Prospecting, 31, 861-872.

Palacky GJ (1987) Resistivity Characteristics of Geologic Targets, in M Nabighian (ed) *Electromagnetic Methods in Applied Geophysics*, Investigations in Geophysics No. 3, Society of Exploration Geophysicists, Tulsa.

Pedersen JB, Schaars FW, Christiansen AV, Foged N, Schamper C, Rolf H and Auken E (2017) Mapping the fresh-saltwater interface in the coastal zone using high-resolution airborne electromagnetics, *First Break*, 35(8), doi:10.3997/1365-2397.35.8.89806.

Reid JE, Pfaffling A and Vrbancich J (2006) Airborne electromagnetic footprints in 1D Earths, *GEOPHYSICS*, 71(2):G63–G72, doi:10.1190/1.2187756.

Sattel, D (1998) Conductivity information in three dimensions. Exploration Geophysics 29, 157-162.

Sattel, D (2005) Inverting airborne electromagnetic (AEM) data with Zohdy's method,: Geophysics, 70 (4), G77-G85.

Sengpiel K and Siemon B (2000) Advanced inversion methods for airborne electromagnetic exploration, *GEOPHYSICS*, 65(6):1983–1992, doi:10.1190/1.1444882.

SkyTEM Australia Pty Ltd (2022) *SKYTEM HELICOPTER EM SURVEY: LIMESTONE COAST AEM SURVEY, PORT MACDONNELL, SA*, Perth, Western Australia.

Sørensen, KI and Auken E (2004) SkyTEM – A new high-resolution helicopter transient electromagnetic system: Exploration Geophysics 35, 191–199.

Spies B and Woodgate P (2004) *Salinity mapping methods in the Australian context*, Academy of Science Natural Resource Minesterial Council, https://www.vgls.vic.gov.au/client/en_AU/vgls/search/detailnonmodal/ent:$002f$002fSD_ILS$002f0$002fSD_ILS:185167/one.

Viezzoli, A, Christiansen, AV, Auken, E and Sørensen, K (2008). Quasi-3D modelling of airborne TEM data by spatially constrained inversion: Geophysics 73, F105–F113.

Viezzoli, A., Auken, E., & Munday, T (2009) Spatially constrained inversion for quasi 3D modelling of airborne electromagnetic data an application for environmental assessment in the Lower Murray Region of South Australia. Exploration Geophysics, 40(2), 173–183. https://doi.org/10.1071/EG08027

Zhao R and and Fan J (2016) Global complexity bound of the Levenberg–Marquardt method, *Optimization Methods and Software*, 31(4):805–814, doi:10.1080/10556788.2016.1179737.

GOYDER INSTITUTE FOR WATER RESEARCH

Government of South Australia
Department for Environment and Water

CSIRO

Flinders University

THE UNIVERSITY of ADELAIDE

University of South Australia

The Goyder Institute for Water Research is a research alliance between the South Australian Government through the Department for Environment and Water, CSIRO, Flinders University, the University of Adelaide and the University of South Australia.